CREIMBO: CROSS-REGIONAL ENSEMBLE INTERACTIONS IN MULTI-VIEW BRAIN OBSERVATIONS

Anonymous authors
Paper under double-blind review

ABSTRACT

Modern recordings of neural activity provide diverse observations of neurons across brain areas, behavioral conditions, and subjects; presenting an exciting opportunity to reveal the fundamentals of brain-wide dynamics. Current analysis methods, however, often fail to fully harness the richness of such data, as they provide either uninterpretable representations (e.g., via deep networks) or oversimplify models (e.g., by assuming stationary dynamics or analyzing each session independently). Here, instead of regarding asynchronous neural recordings that lack alignment in neural identity or brain areas as a limitation, we leverage these diverse views into the brain to learn a unified model of neural dynamics. Specifically, we assume that brain activity is driven by multiple hidden global sub-circuits. These sub-circuits represent global basis interactions between neural ensembles—functional groups of neurons—such that the time-varying decomposition of these sub-circuits defines how the ensembles' interactions evolve over time non-stationarily and non-linearly. We discover the neural ensembles underlying non-simultaneous observations, along with their non-stationary evolving interactions, with our new model, **CREIMBO** (Cross-Regional Ensemble Interactions in Multi-view Brain Observations). CREIMBO identifies the hidden composition of per-session neural ensembles through novel graph-driven dictionary learning and models the ensemble dynamics on a low-dimensional manifold spanned by a sparse time-varying composition of the global sub-circuits. Thus, CREIMBO disentangles overlapping temporal neural processes while preserving interpretability due to the use of a shared underlying sub-circuit basis. Moreover, CREIMBO distinguishes session-specific computations from global (session-invariant) ones by identifying session covariates and variations in sub-circuit activations. We demonstrate CREIMBO's ability to recover true components in synthetic data, and uncover meaningful brain dynamics in human high-density electrode recordings—capturing cross-subject neural mechanisms as well as inter- vs. intra-region dynamical motifs.

1 INTRODUCTION

Identifying the interactions between and within brain areas is fundamental to advancing our understanding of how the brain gives rise to behavior. Recent advances in neural recording present an exciting opportunity to study brain-wide interactions by enabling simultaneous recording of neural activity across many brain areas through multiple high-density electrodes. Such experiments, repeated over many sessions with different implantation patterns, offer multiple asynchronous recordings of the brain system, with each session encompassing hundreds of distinct neurons across regions.

Individual recording sessions provide a singular perspective of the brain dynamics, as the reinsertion of recording devices results in the capture of different subsets of neurons in each session. Thus, fitting population-level models often reverts to per-session analysis (i.e., fitting each session independently), which is inherently constrained by the inability to incorporate the full set of recorded activity across all recorded brain areas across all sessions. Moreover, analyzing the data session-by-session, may hinder our ability to distinguish between computations that are session or subject specific from task related or global session-invariant neural processes. Compounding the difficulty of merging different sessions' data are the non-linear and non-stationary nature of neural activity, as well as the presence of noise and variability across trials—both of which require additional model complexity to account

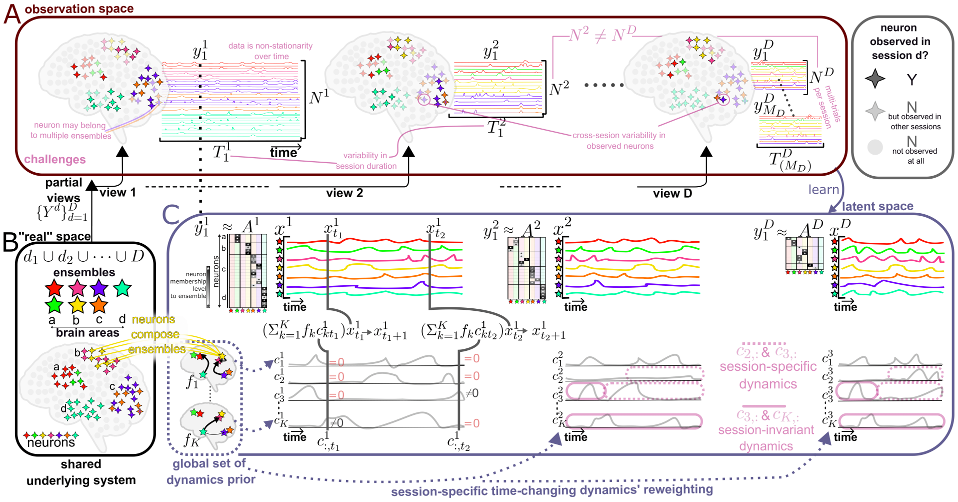
A
observation space
y_1^1
data is non-stationarity over time
N^1
neuron may belong to multiple ensembles
challenges
T_1^1
time
variability in session duration
y_1^2
N^2
T_1^2
$N^2 \neq N^D$
cross-sesion variability in observed neurons
y_1^D
N^D
$y_{M_D}^D$
multi-trials per session
$T_{(M_D)}^D$
neuron observed in session d?
Y
N but observed in other sessions
N not observed at all
partial views
$\{Y^d\}_{d=1}^D$
view 1
view 2
view D
learn
latent space
B
"real" space
$d_1 \cup d_2 \cup \cdots \cup D$
ensembles
a b c d
brain areas
neurons compose ensembles
a
b
c
d
neurons
shared underlying system
C
$y_1^1 \approx A^1$
neuron membership level to ensemble
neurons
x^1
$x_{t_1}^1$
$x_{t_2}^1$
time
$(\Sigma_{k=1}^K f_k c_{kt_1}^1) x_{t_1}^1 \rightarrow x_{t_1+1}^1$
$(\Sigma_{k=1}^K f_k c_{kt_2}^1) x_{t_2}^1 \rightarrow x_{t_2+1}^1$
$y_1^2 \approx A^2$
x^2
$y_1^D \approx A^D$
x^D
f_1
f_K
c_1^1
c_2^1
c_3^1
c_K^1
$=0$
$\neq 0$
$c_{:,t_1}^1$
$c_{:,t_2}^1$
c_1^2
c_2^2
c_3^2
c_K^2
$c_{2,:}$ & $c_{3,:}$: session-specific dynamics
$c_{3,:}$ & $c_{K,:}$: session-invariant dynamics
c_1^3
c_2^3
c_3^3
c_K^3
global set of dynamics prior
session-specific time-changing dynamics' reweighting

Figure 1: **CREIMBO's Illustration. A:** Real-world multi-regional neural datasets consist of multiple (D) non-simultaneous recording sessions ($\{\boldsymbol{Y}^d\}_{d=1}^D$) that cannot be matched in terms of individual neurons' identities, quantity, or cross-region distribution, resulting in neurons appearing only in certain sessions (4-pointed stars) or not at all (gray circles). This variability hinder our ability to draw unified conclusions of whole-brain neural computation, while analyzing sessions individually could lead to session-specific biased results. This challenge is further complicated by variability in session (or trial) duration, the non-stationarity of brain dynamics (even within a session), and the presence of multiple trials within each session. **B** → **A:** Instead of considering these asynchronous sessions as a challenge, we frame them as an opportunity to obtain distinct, potentially complementary "views" onto the shared underlying brain system, thereby facilitating the learning of a unified brain dynamics model. We assume that brain computations are mediated by multiple neural ensembles—★ groups of same-region neurons with shared functionalities—whose interactions yield meaningful neural representations. However, the specific neurons and their membership degrees within each ensemble are unknown, and a neuron may belong to multiple ensembles with varying membership levels based on its diverse functionalities. **C:** CREIMBO leverages partial brain views to co-learn ensemble compositions per session ($\{\boldsymbol{A}^d\}_{d=1}^D$), their temporal activity ($\{\boldsymbol{x}^d\}_{d=1}^D$), and cross-regional interactions $\boldsymbol{x}_{t+1}^d = \boldsymbol{F}_t^d \boldsymbol{x}_t^d$. It posits that these non-stationary interactions stem from a session-shared dictionary prior of up to K global interactions $\{\boldsymbol{f}_k\}_{k=1}^K$, whose sparse time-changing decomposition $\boldsymbol{F}_t^d = \sum_{k=1}^K \boldsymbol{f}_k \boldsymbol{c}_{kt}^d$ shapes the overall ensemble dynamics at each time point t and session d. The interactions' coefficients can help distinguish session-specific interactions from session-invariant interactions in different time periods (pink right, solid vs. dotted in subplot C right). With the session-shared ensemble-interactions dictionary and certain assumptions (Sec. D), the model auto-sorts ensembles across sessions by functionality, aligning the j-th ensemble of session d with the j-th ensemble of session d', despite differences in observed neurons.

for. Moreover, to extract scientifically meaningful insights, the models must be interpretable, with model parameters directly related to task variables or connections between recorded units. This gap between the opportunities offered by modern neural data and the limited capabilities of current methods necessitates new approaches to leverage the richness in modern brain data and discover the fundamental neural sub-circuits governing brain activity.

One current approach used to combine multi-session data into unified model is deep learning. By training to predict all sessions' data, deep networks implicitly merge the datasets into the fit network weights. While these powerful models can combine information across sessions, their uninterpretable nature and complexity typically hinders their ability to reveal the fundamental building blocks of neural computation. Other approaches, including tensor factorization and its variations (e.g., Chen et al. (2015); Harshman (1970)) may be limited in their ability to merge sessions of varying durations or model the interactions between the identified neural components.

Here, we re-frame cross-session variability in neurons recorded and experimental settings, not as a drawback, but as a valuable advantage, viewing this data as providing multiple, complementary "views" into a single, shared brain system (Fig. 1B → A). This approach enables a more thorough and holistic discovery of the underlying system designed to extract joint information from the entire dataset. In particular, we hypothesize that the population dynamics at each session is driven by a common set of global time-invariant sub-circuits shared across sessions. To effectively capture the non-linear and non-stationary dynamics of the brain, we enable these sub-circuits to adjust their activity levels over time and across sessions. This approach allows us to identify evolving neural patterns through the collective activity of the sub-circuits, modeled via their time-varying decomposition. We assume that the latent dynamics governed by functional neural groups are shared across sessions, even though the specific individual neurons observed may vary. To address this, we propose a per-session transformation from the joint low-dimensional circuit space to each session's observation space, ensuring cross-session alignment of the neural groups' functionalities.

In this work, we lay out this new model, which we term **C**ross-**R**egional **E**nsemble **I**nteractions in **M**ulti-view **B**rain **O**bservations (CREIMBO), and demonstrate its ability to capture latent dynamics in multi-view neural data. Specifically, our contributions include:

- We discover multi-regional brain dynamics through leveraging the richness of modern neural datasets while ensuring interpretability.
- We distinguish between intra- and inter-region interactions by identifying sparse, same-area neural ensembles, deploying a specialized structured prior over per-session projections from the circuit latent space to the observed neural space.
- We accurately recover ground truth components in synthetic data and discover meaningful cross-regional brain interactions underlying human and mouse brain data.

2 RELATED WORK

Over the past decade, remarkable advances in neural data acquisition technologies have enabled the measurement of numerous neurons across brain regions, subjects, and experimental settings. This has spurred follow-up work to leverage this extensive data for novel neural discoveries, including merging non-simultaneous sessions and examining cross-regional brain interactions, all while accounting for the complex, non-linear, and non-stationary nature of neural activity.

Merging non-simultaneous neural recording sessions. Existing work for combining non-simultaneous neuronal population recordings, here termed "sessions", include Turaga et al. (2013) who introduced the term "stitching" for this problem and modeled neural activity with a shared latent dynamical systems model and Soudry et al. (2013) who proposed to stitch asynchronous recordings for inferring functional connectivity by assuming shared cross-session latent input and demonstrated the advantage in observing more neurons for inferring connectivity. However, these methods are not designed to capture more than two simultaneously interacting neural sub-circuits across multiple populations, nor do they distinguish between within- and between-area interactions or specifically address temporal non-stationarity. Bishop (2015) and Bishop & Yu (2014) proposed integrating the neural activity structure into inference and expanding stitching to study the communication between two neuronal populations from potentially different brain areas. In Nonnenmacher et al. (2017), the authors proposed extracting low-dimensional dynamics from multiple sessions by learning temporal co-variations across neurons and time. Both of these methods, through, assume at least a small overlap in the identity of cross-session observed neurons. LFADS (Keshtkaran et al., 2021; Pandarinath et al., 2018) enables stitching while addressing the need for limited neural overlap by finding a shared non-linear latent dynamical model. However, its latent dynamics may be difficult to interpret regarding the specific neural sub-circuits that compose it, and due to its foundation on a variational auto-encoder, it may be challenging to tune.

Maintaining Interpretability in Non-Stationary Neural Dynamics Models. Real-world neural activity follows non-stationary nature due to changing environmental settings. Classical dynamical models often simplified neural dynamics to linear (e.g., jPCA Churchland et al. (2012)) or non-linear but stationary (e.g., Gallego et al. (2020)). Models that capture non-stationarity often derive from "black box" deep learning models (e.g., Schneider et al. (2023); Pandarinath et al. (2018); Zhu et al. (2022), which are powerful but often present limited interpretability with respect to neural interactions. Other models are built on switching piece-wise linear models Linderman et al. (2016; 2017); Murphy (1998), which do not enable the identification of multiple co-active dynamic processes. dLDS (decomposed Linear Dynamical Systems, Mudrik et al. (2024a)) and its multi-step extension (Mudrik et al., 2024c)), addresses this gap by generalizing the switching assumption to sparse time-changing decomposition of linear dynamical systems, thus enabling capturing co-active sub-circuits. However, while dLDS can be extended to co-process multi-session recordings with cross-session variability in neuron identity, this modification may not yield interpretable latent-to-observed projections and lacks the structured multi-regional prior over the emission matrix necessary to partition multi-area recordings and study between- vs. within-area interactions.

Identification of Functional Neural Ensembles. A potential way to find interpretable loading matrix that links low to high dimensional space is through the identification of functional neural ensembles—here referred to as groups of neurons with similar functionalities—that determine the axes in the latent space. For instance, the mDLAG model used Automatic Relevance Determination (ARD) to promote population-wise sparsity patterns of each latent variable. In Mudrik et al. (2024b), the authors presented an approach to address sparsity in loading matrices while accounting for multi-trial and task-conditions variability. They proposed a graph-driven regularization technique that facilitates the grouping of co-active neurons into the same ensembles and pushing apart neurons that present different functionality, while allowing for structural adjustments in ensemble configurations across different task conditions. They further enable per-trial variability in temporal activity of the ensembles. However, their model does not model the dynamic interactions between ensembles or give a closed form prior for the evolution of the ensembles' temporal traces. While other methods, e.g., clustering approaches like (Grossberger et al., 2018) or Sparse Principal Component Analysis (SPCA) Zou et al. (2006), enable the recognition of underlying sparse groups, they either do not allow a neuron to belong to multiple groups with varying degrees of membership or do not support controlled adaptations of structural membership across conditions.

Multi-regional brain interactions. With the ability to record from multiple brain areas and the recognition of the importance of considering multi-area communication (Pesaran et al., 2021), recent works have delved into understanding the communication between or within brain areas. In Gokcen et al. (2022; 2024), the authors proposed models to identify time delays between cross-regional brain interactions, overcoming the challenge of distinguishing indirect, concurrent, and bi-directional interactions in two or more populations. However, their model focuses on analyzing sessions individually and is not intended to uncover the full underlying set of transition matrices, but rather to recognize meaningful time delays that can imply interactions. Other models addressed multi-regional interactions through a communication subspace Semedo et al. (2019) using dimensionality reduction, or by Generalized Linear Models (GLMs), with either Poisson (Yates et al., 2017) or Gaussian (Yates et al., 2017) statistics to identify functional coupling between areas. These approaches, though, are not tailored to capture non-simultaneous cross-sessions variability in neuron identity and subject processing. Other recent methods (Karniol-Tambour et al. (2024); Glaser et al. (2020); Li et al. (2024)) discussed the potential usage of their model to multi-regional interactions, have proposed studying multi-regional interactions using switching dynamical systems approaches, where the model switches between different states over time to capture distinct periods. However, this approach cannot disentangle interactions among multiple sub-circuits active simultaneously, nor can it identify interactions at multiple temporal resolutions that occur concurrently and distinguish between these or multiple co-processed processes whose encoding occurs gradually rather than via sharp transitions.

3 PROBLEM INTRODUCTION AND APPROACH

Problem Intuition: Let $\{\boldsymbol{Y}^d\}_{d=1}^D$ be a set of estimated neural firing rates (e.g. from neuropixels data) over D asynchronous sessions, indexed by $d = 1 \dots D$. The neural recordings of each d session, $\boldsymbol{Y}^d \in \mathbb{R}^{N^d \times T^d}$, capture T^d time observations of the activity of N^d neurons from up to J distinct brain areas, thus offering a partial view of the brain system. Note that sessions may refer to the same or different subjects, can vary in duration or number of neurons, i.e. N^d and T^d need not be equal to $N^{d'}$ and $T^{d'}$ for different sessions d, d', and can differ in the subset of brain areas (out of J) they capture. Hence, these cross-session data matrices cannot be aligned into a single data array, e.g., via a tensor—hindering the direct application of existing analyses as tensor factorization.

We assume that these brain observations reflect the hidden activity $\boldsymbol{X}^d \in \mathbb{R}^{p \times T^d}$ of $p << N^d$ functional neural groups that evolve and interact over time. Each of these groups encompasses a sparse set of same-area neurons, while each neuron can belong to more than one group with varying degrees of cross-group membership, encoded in the values of $\boldsymbol{X}^d$. The low-dimensional latent space in which the groups interact is shared across sessions and projected to each session's observed neurons via an unknown per-session projection $g^d : \mathbb{R}^p \to \mathbb{R}^{N^d}$ that captures the groups' compositions in the visible neurons, such that $\boldsymbol{Y}^d = g^d(\boldsymbol{X}^d)$. The interactions between these functional groups follow a per-session non-linear and non-statioary dynamics $\boldsymbol{F}_t^d : \mathbb{R}^p \to \mathbb{R}^p$, where $\boldsymbol{X}_t^d = \boldsymbol{F}_t^d(\boldsymbol{x}_{t-1}^d)$. As in general non-stationary systems cannot be fit without constraints, we follow the dLDS model and assume that these dynamics can be described by a set $\{\boldsymbol{f}_k\}_{k=1}^K$ of K global time- and session-invariant "sub-circuits". Here each sub-circuit $\boldsymbol{f}_k \in \mathbb{R}^{p \times p}$ represents a basis interaction between these groups that is reused by the system at different time-points throughout its trajectory. Each of these latent sub-circuits may capture either "global" session-invariant brain interactions and/or session- and subject-specific interactions. Moreover, these sub-circuits may be active simultaneously or intermittently, yielding a model that can flexibly fit neural trajectories that differ between sessions with a single underlying mechanism. The problem CREIMBO addresses is thus identifying the set of K latent multi-regional sub-circuits $\{\boldsymbol{f}_k\}_{k=1}^K$, capturing interactions between unknown functional sparse neural ensembles $\boldsymbol{A}$, along with their non-stationary activation levels $\{\{\boldsymbol{c}_{\boldsymbol{kt}}^{\boldsymbol{d}}\}_{k=1}^K\}_{d=1}^D$, by leveraging the joint information from asynchronously collected observations $\{\boldsymbol{Y}^d\}_{d=1}^D$.

CREIMBO: A naive approach to identifying the unknown sub-circuits involves first projecting each session's data into a low-dimensional space and subsequently fitting the dynamics model in the low-dimensional space. However, this two-step approach can be sub-optimal as the dimensionality reduction projections may not prioritize the same dimensions needed to preserve dynamic fidelity. An additional advantage of simultaneously identifying the ensembles and dynamics is that in the cross-session model it automatically aligns the cross-session components based on the shared dynamics prior. Such alignment is unlikely given the sensitivity of the subspace ordering in dimensionality reduction methods to each session's distinct statistics.

We therefore present CREIMBO, an algorithm that simultaneously fits the global sub-circuits that underlie the inter-ensemble interactions across multiple sessions. Our model is predicated on three key assumptions that 1) ensembles of neurons, rather than individual neurons, form the basic units that interact in brain dynamics, 2) it is feasible to identify functionally analogous neuronal ensembles across sessions, and 3) the full repertoire of interactions between these ensembles are governed by a global set of dynamical primitives in the form of a basis of linear dynamical systems.

Let $\boldsymbol{A}^d$ be a sparse matrix where each column, $\boldsymbol{A}^d[:, j]$, encodes the neuronal composition of the j-th ensemble in the d-th session, such that non-zero values within these columns represent the membership of neurons in the ensemble and their magnitudes reflecting the degree of membership. Since we aim to capture multi-regional interactions, we design the ensemble matrix $\boldsymbol{a} := \boldsymbol{A}^d$ as a block diagonal matrix where the j-th block, $\boldsymbol{a}^j \in \mathbb{R}^{n_j \times p_j}$, contains the neural ensembles for the j-th area. We denote p_j as the number of ensembles within that area (note that $p = \sum_{j=1}^J p_j$) and $n_j := N_j^d$ as the number of neurons in that area (i.e., the total number of neurons observed in session d is $N^d = \sum_{j=1}^J n_j$). Furthermore, let $\tau := \mathrm{T}_m^d$ indicate the number of time-points recorded in each m-th trial of session d ($m = 1 \ldots M_d$), such that the observations in that trial are captured by $\boldsymbol{Y}_m^d \in \mathbb{R}^{N^d \times \mathrm{T}_m^d}$. In each trial m, the temporal activity for the p ensembles are denoted as $\boldsymbol{x} := \boldsymbol{X}_m^d \in \mathbb{R}^{p \times \tau}$, leading to a model where the observations $\boldsymbol{y} := \boldsymbol{Y}_m^d$ in trial m are assumed to arise from the joint activity of all these ensembles, up do a normally-distributed error $\epsilon \sim \mathcal{N}(0, \sigma)$, i.e., $\boldsymbol{y} = \boldsymbol{a}\boldsymbol{x} + \epsilon$. Please refer to Section G for Poisson statistics inference in low spiking rate regimes. The evolution of the ensembles' activities ($\boldsymbol{x}$) reflect the latent interactions between ensembles, which we model with a non-stationary linear dynamical system $\boldsymbol{x}_t = \boldsymbol{F}_t \boldsymbol{x}_{t-1}$ for $t = 1 \ldots \tau$. The time-changing transition matrix $\boldsymbol{F}_t \in \mathbb{R}^{p \times p}$ captures both non-linear and non-stationary brain activity. A key desired property of our model is to capture the overlapping activity of multiple sub-circuits of interacting ensembles. We thus follow dLDS and model the interactions ($\boldsymbol{F}_t$) through a time-varying sparse decomposition $\boldsymbol{F}_t = \sum_{k=1}^K \boldsymbol{c}_{kt} \boldsymbol{f}_k$, where $\{\boldsymbol{f}_k\}_{k=1}^K$ are the K global ensemble interactions, and $\boldsymbol{c}_{kt}$ are their time-varying coefficients that capture the modulation of each interaction.

Fitting this model requires identifying the global operators $\{\boldsymbol{f}_k\}_{k=1}^K$ and ensembles $\{\boldsymbol{A}^d\}_{d=1}^D$. For this, we employ an alternating approach and iterate between updating $\{\boldsymbol{f}_k\}_{k=1}^K$ and inferring, for each session d, 1) the ensemble compositions $\boldsymbol{a} := \boldsymbol{A}^d$, 2) their dynamics $\boldsymbol{x}$, and 3) the sub-circuits' temporal coefficients $\boldsymbol{c}_t$. These steps are iterated until convergance.

Ensemble update: We update $\boldsymbol{a}$ per-row (neuron) n ($\boldsymbol{a}_n$). Following the work of Mudrik et al. (2024b), we infer the sparse ensemble structures with graph-driven re-weighted ℓ_1 regularization that groups together neurons with shared activity patterns, while pushing apart neurons who do not behave similarly. The graph for each area j, $\boldsymbol{h}^j \in \mathbb{R}^{n_j \times n_j}$, is calculated based on a data-driven Gaussian kernel that measures the temporal similarity between neurons, such that $\boldsymbol{h}^j_{n1,n2} = exp(\frac{\|\boldsymbol{y}^j_{n1} - \boldsymbol{y}^j_{n2}\|_2^2}{\sigma_h})$ where σ_h is a hyperparameter. Specifically, for each row $\boldsymbol{a}_{n,:}$ and considering only the ensembles in region j_n that neuron n is part of,

$$\widehat{\boldsymbol{a}}_{n,:} = \arg\min_{\boldsymbol{a}_{n:}} \|\boldsymbol{y}_{n:} - \boldsymbol{a}_{n:}\boldsymbol{x}_{j_n:}\|_2^2 + \sum_{j=1}^{p} \boldsymbol{\lambda}^d_{n,j} |\boldsymbol{a}_{n,j}| \text{ where } \boldsymbol{\lambda}_{n,j} = \frac{\beta_1}{\beta_2 + |\widehat{\boldsymbol{a}}_{n,j}| + \beta_3 |\boldsymbol{h}^j_{n:}\widehat{\boldsymbol{a}}_{:j}|}. \quad (1)$$

Here, $\boldsymbol{x}_{j_n,:}$ is the activity of the ensembles of the j_n-th region and β_1, β_2, and β_3 are scalars that control the effect of the graph on the regularization. The graph adjacency $\boldsymbol{h}_{n:}\widehat{\boldsymbol{a}}_{:j}$ weights the sparse membership in the j-th ensemble based on temporal similarity. Specifically, if $\boldsymbol{h}_{n:}\widehat{\boldsymbol{a}}_{:j}$ is high (i.e., the neighbors neuron n on the graph are in the current estimate of the j-th ensemble), $\boldsymbol{\lambda}_{n,j}$ is small, resulting in lower sparsity regularization on neuron n for that ensemble, promoting it to be included. Alternatively, if this correlation is small, the regularization weight $\boldsymbol{\lambda}_{n,j}$ is large, and neuron n will be more likely not to be included in ensemble j.

Latent state and dynamics coefficient update: The ensemble activities $\boldsymbol{x}$ and coefficients $\boldsymbol{c}$ are updated iterative for each time-point t via the LASSO optimization

$$\widehat{\boldsymbol{x}}_t, \widehat{\boldsymbol{c}}_t = \arg\min_{\boldsymbol{x}_t, \boldsymbol{c}_t} \|\boldsymbol{y}_t - \boldsymbol{a}\boldsymbol{x}_t\|_2^2 + \left\| \boldsymbol{x}_t - \left(\sum_{k=1}^{K} \boldsymbol{f}_k \boldsymbol{c}_{k,(t-1)} \right) \boldsymbol{x}_{t-1} \right\|_2^2 + \lambda_c \|\boldsymbol{c}_t\|_1 \quad (2)$$

where $\lambda_c \in \mathbb{R}$ is sparsity-regularization weights on the basis interactions' activations.

Dynamical system update: The global ensembles interactions, $\{\boldsymbol{f}_k\}_{k=1}^K$ are assumed to be sparse (i.e. ensembles interactions are not all to all) and are identified directly by:

$$\boldsymbol{F}^{\text{all}} = \arg\min_{\boldsymbol{F}^{\text{all}}} \|\boldsymbol{x}^+ - \boldsymbol{F}^{\text{all}}(\boldsymbol{cx})\|_2^2 + \lambda_F \|\text{vec}(\boldsymbol{F}^{\text{all}})\|_1 + \lambda_\rho \sum_{k_1, k_2, (k_1 \neq k_2)} \rho(\boldsymbol{f}_{k_1}, \boldsymbol{f}_{k_2}) \quad (3)$$

where $\boldsymbol{F}^{\text{all}} \in \mathbb{R}^{p \times pK}$ is an horizontal concatenation of all $\boldsymbol{f}$s, and $\boldsymbol{x}^+ \in \mathbb{R}^{p \times \sum_{d \in \text{batch}} \mathrm{T}^d}$ is the horizontal concatenation of all $\{\{\boldsymbol{x}^d_{t+1}\}_{t=1}^{\mathrm{T}^d}\}_{d \in \text{batch}}$, where "batch" means that this operation is in practice taken on a random subset of sessions for computational complexity considerations. Above, $\boldsymbol{cx}^{\text{batch}}_t \in \mathbb{R}^{Kp \times 1} = [(\boldsymbol{c}^d_t \otimes [1]_{1 \times p}) \circ ([1]_{1 \times K} \otimes \boldsymbol{x}^d_t)^T]^T$, such that $\boldsymbol{cx} \in \mathbb{R}^{Kp \times \sum_{d \in \text{batch}} \mathrm{T}^d}$ is the horizontal concatenation of all $\{\{(\boldsymbol{cx})^d_t\}_{t=1}^{\mathrm{T}^d}\}_{d \in \text{batch}}$. The operator vec$(\cdot)$ flattens a matrix to a vector and λ_F is ℓ_1 sparsity-promoting weight on $\boldsymbol{F}^{\text{all}}$. $\rho(\cdot)$ represents correlation, such that $\sum_{k_1,k_2} \rho(\boldsymbol{f}_{k_1}, \boldsymbol{f}_{k_2})$ is a de-correlation term with weight λ_ρ used to ensure that distinct $\boldsymbol{f}$s are not too similar. See Algorithm 1 for a method summary and Section E for complexity analysis.

4 EXPERIMENTS

CREIMBO recovers Ground Truth Components in Synthetic Data: We first assess CREIMBO's ability to recover ground-truth components from synthetic data. We generated $K = 3$ sub-circuits represented by a set of 3 rotational matrices (Fig. 5B). These sub-circuits capture interactions among $p = 3$ ensembles from $J = 3$ regions ($p_j = 1$ for all $j = 1, \dots, J$). Each region consists of a random number of neurons drawn from a uniform distribution between 4 to 9. We finally generated the data by simulating 5 sessions with different neuron identities and varying numbers of neurons per region(Fig. 5A and D). CREIMBO was able to recover the ground truth components with high accuracy, as measured by correlation with the ground truth, across 312 random noisy initialization repeats with random parameters from a range described in 1. Accurate recover included all parameters: the reconstructed observations $\boldsymbol{y}$ (Fig. 2A), ensemble composition $\boldsymbol{A}$ (Fig. 2B) and activity $\boldsymbol{x}$ (Fig. 2C), sub-circuits $\boldsymbol{F}$ (Fig. 2D), and coefficients $\boldsymbol{c}$ (Fig. 2E). Comparing CREIMBO's results to components identified under diverse ablations (details in D), we found that approaches that either separate the ensembles and dynamics identifications steps, analyze each session separately, or do not consider the localized structure of the ensembles, fail to recover the ground-truth components, i.e., the resulting fit model parameters are less correlated with the ground-truth observations (Fig. 2F-J, 7).

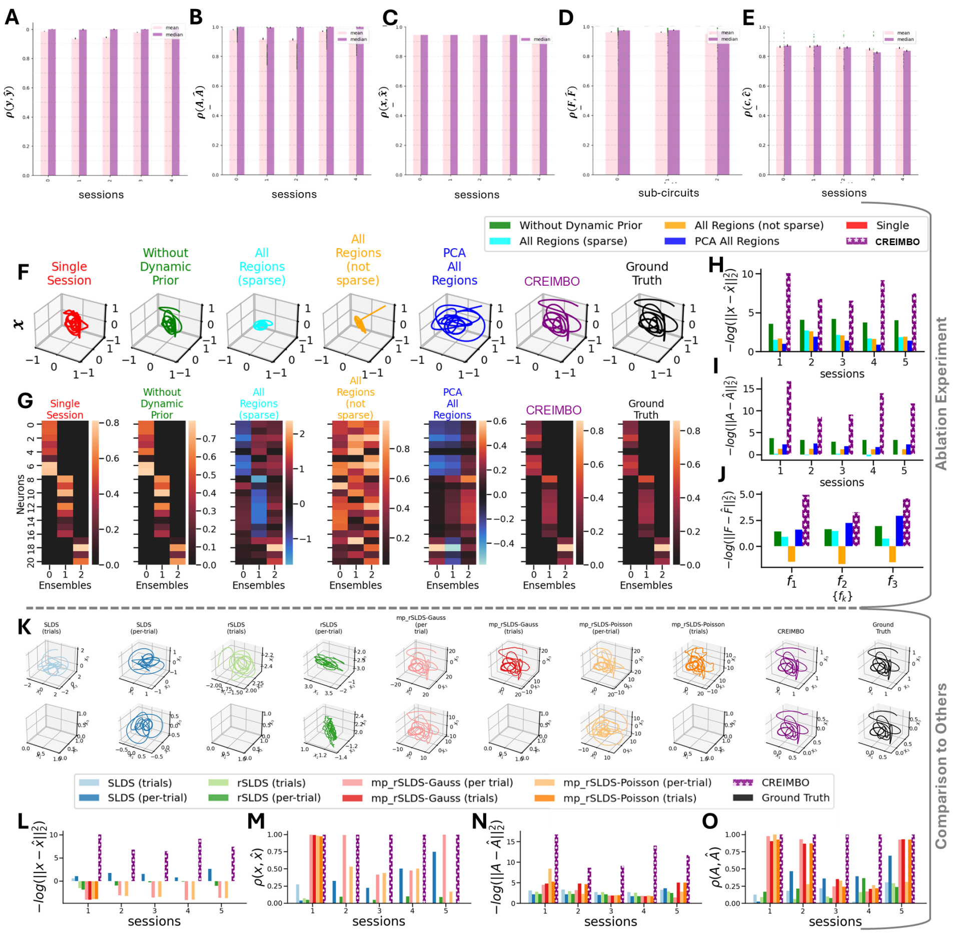

Figure 2: **A-E:** Testing CREIMBO over 312 repeats with varying random initializations and random seeds (Sec. B) reveals high correlations between ground truth and fit components for all unknowns, $\boldsymbol{Y}$, $\boldsymbol{A}$, $\boldsymbol{x}$, $\boldsymbol{F}$, $\boldsymbol{c}$ (subplots **A-E** respectively). **F-G:Ablation Experiment:** Comparison of the ensemble trajectory ($\boldsymbol{x}^d$, subplot F) and the ensemble compositions ($\boldsymbol{A}$, subplot G) for the 1-st session as identified by CREIMBO vs. various ablations (details in Sec. D, see Figure 7 for more sessions). **H-J:** Comparing CREIMBO to ablation variants in terms of $-\log(\text{MSE})$ between the ground truth and identified latent dynamics, ensemble composition, and sub-circuits entries. **K: Baseline Comparisons:** the latent dynamics identified by the baselines (SDLS, rSLDS (Linderman et al., 2016), multi-population rSLDS (Glaser et al., 2020), details in Sec. D) for the first two sessions (merged sessions baselines provide a single trajectory). **L-O:** Comparison of the latent dynamics and identified ensemble matrices compared to the ground truth across the baselines.

We further evaluated CREIMBO's ability to recover hidden components compared to other methods, (Fig. 2 K-O, Fig.8. baselines details in Sec. D). While the latter shows improved performance, CREIMBO more accurately recovers the ground truth hidden dynamics and ensembles. Importantly, these models are not designed to identify multiple co-occurring processes or sparse ensembles, in contrast to CREIMBO, and they are not suitable for multi-sessions with varying neural identities, which limits the comparison from the outset.

Next, we tested CREIMBO on a richer synthetic example with $D = 15$ sessions. Each session had a varying number of neurons (a random integer between 14 and 19 per region from a uniform distribution) and distinct sub-circuit coefficients (see Fig. 11 for the generated ground truth components and 9 for regional distributions and masking). The sub-circuits were set as rotational matrices, similar to the previous experiment. Over 204 random initializations with different parameters (see Sec. B) we again found that CREIMBO robustly identifies the ground truth latent dynamics, ensemble compositions, and sub-circuits. Moreover, CREIMBO accurately reconstructed the observations with high correlation to the ground truth across all initializations (Fig. 11E) with low

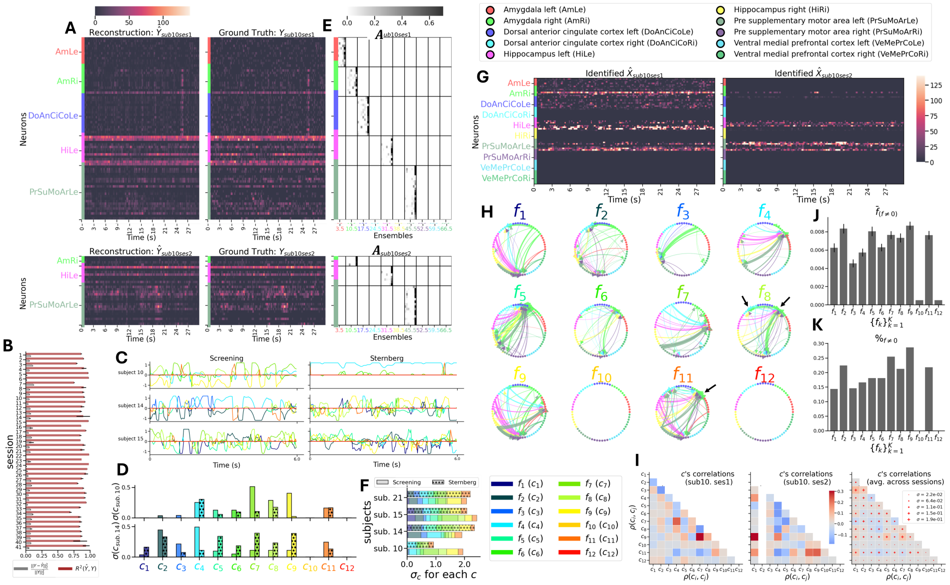

Figure 3: CREIMBO identifies cross-regional neural sub-circuits underlying multi-session human brain recordings. **A:** Two exemplary observations ($\boldsymbol{Y}$, right) compared to their reconstruction by CREIMBO ($\widehat{\boldsymbol{Y}}$, left). **B:** Reconstruction performance in terms of R^2 and relative error across all sessions. **C:** The sub-circuit coefficients for 3 exemplary subjects. **D:** The standard deviation (std) of the coefficients over time across the two exemplary sessions. **E:** Exemplary identified sparse ensemble matrices ($\{\boldsymbol{A}^d\}_{d=1}^{D}$) for the observations from **A**. **F:** Relative std of the coefficients across four subjects reveals usage of similar sub-circuits. **G:** The identified ensembles' activity ($\boldsymbol{X}^d$) for the two exemplary sessions. **H:** The identified sub-circuits. Width indicates effect magnitude. Each circle corresponds to an ensemble with its color indicating the ensemble's area. Black arrows near $\boldsymbol{f}_8$ and $\boldsymbol{f}_{11}$ highlight within-region interactions. **I:** Pairwise correlations between within-session sub-circuit coefficients (left, middle) and average within-session correlations across all sessions. STD marked by "+" marker size. **J:** Mean and STD of connections fs. **K:** Number of non-zero connections per $\boldsymbol{f}_k$.

relative error (Fig. 11F). We further tested CREIMBO on more advanced data that included $D = 40$ sessions with a maximum of 4 regions and $p_j = 3$ ensembles per region (Fig. 12). We found that CREIMBO manages to recover the components with high correlation with the ground-truth (Fig 13).

CREIMBO Discovers Multi-Regional Dynamics in Electrophysiology Data: We then tested CREIMBO on human neural recordings from a high-density electrode array provided by Kyzar et al. (2024). The data consists of neural activity from overall $p = 10$ brain areas with limited cross-session regional overlap (Fig. 14, 15), recorded while subjects performed a screening task (details in Kyzar et al. (2024)). The data encompasses 21 subjects across $D = 41$ non-simultaneous sessions. For each subject (except Subject 19), the data offers 1) a "Screening" session, and 2) a "Sternberg test" session (details in Kyzar et al. (2024)). We first converted the spike-sorted units to firing rate matrices by convolving the spike trains with a 30ms Gaussian kernel (Fig. 10), and then tested CREIMBO on all sessions together with a maximum of $K = 12$ sub-circuits and as most $p_j = 7$ ensembles per region (full parameter list in Tab. 2). First we note that CREIMBO can accurately reconstruct the data with high accuracy across all sessions (Fig. 3A, B). Interestingly, the ensemble compositions identified by CREIMBO (Fig. 3E) present sparse patterns with one dense ensemble for most regions that we hypothesize capture the "background" mean field activity of that region (right-most column of diagonal blocks in Fig. 3E). The sparse ensembles we hypothesize capture the more specialized, nuanced functionality. The ensembles activity ($\boldsymbol{X}^d$, Fig. 3G) reveal some constantly-active ensembles, implying these neuron groups are important for neural processing.

The universal sub-circuits ($\{\boldsymbol{f}_k\}_{k=1}^{K}$) exhibit distinct localized motifs (Fig. 3H), i.e., most sub-circuits present clear trends of either sourcing or targeting the same area. This is in contrast to other approaches (Sec. D), that yield overlapping uninterpretable sub-circuits (Fig. 22) that emphasize only limited circuitry (Fig. 24). Interestingly, sub-circuits 10, 12 ended up almost empty (mainly zero-ish values, Fig. 3H, 19). This highlights CREIMBO's ability to automatically nullify redundant sub-circuits—i.e., a form of model selection—via the sparsity regularization. The number of active connections and average connection strength (Fig. 10J, K) show modest variability between sub-circuits, highlighting the model's ability to identify distinct sub-circuits with varying interaction resolutions, including those of varying strengths rather than being limited to just k-sparse sub-circuits. From a neuroscience perspective, this suggests that underlying neural sub-circuits can vary in density and the number of participating areas and ensembles. Interestingly, most identified interactions occur between distinct areas (i.e., inter-regional interactions) with either multiple ensembles from the same area affecting together ensembles from a different area (e.g., $\boldsymbol{f}_3$), or multiple ensembles from diverse areas converging to the same target area (e.g., $\boldsymbol{f}_5$). However, these source or target groups of ensembles vary across sub-circuits, hence the full repertoire of activity cannot be captured by a single one, highlighting the importance of CREIMBO's capacity to disentangle the combined activity of multiple circuits. We also observe, but to a lesser degree, within-area interactions (e.g., black arrows in $\boldsymbol{f}_8$, $\boldsymbol{f}_{11}$). These dynamics emphasize that within-area amplification or regulation do exist in addition to global cross-region computations. When exploring the activation patterns of these identified sub-circuits (Fig. 3D, Fig. 20), CREIMBO reveals cross-subject and cross-session variability. Notably, some sub-circuits are consistently used with high variability over time (e.g., $\boldsymbol{f}_8$ light-green), while others, such as $\boldsymbol{f}_{12}$, are not utilized at all in any exemplary session (Fig. 3C, F, e.g., $\boldsymbol{f}_{12}$). Moreover, when exploring sub-circuits with high activity variability across sessions (Fig. 3D,F), we observe that some are used within-subjects but across both tasks (e.g., $\boldsymbol{f}_2$ in subject 14, Fig. 3D), while others are shared across both subjects and tasks (e.g., $\boldsymbol{f}_{11}$, used by subjects 10 and 14 in both task phases). The analysis of within-session pairwise correlations between sub-circuit coefficients (Fig. 10I) reveals low correlations (<0.1) for most pairs. This indicates that the activities of distinct sub-circuits differ and reflect different cognitive processes.

Using these real-world recordings, we further tested CREIMBO's robustness to increasing noise levels (now with $K = 8$ sub-circuits, $p_j = 6$ max ensembles per area) by adding random Gaussian noise pre-training and then training CREIMBO on the noisy data (Fig.23). While CREIMBO remains robust under increasing noise ($\frac{\sigma_{\text{noise}}}{\sigma_{\text{data}}} \sim 0.2$, depending on the parameter of interest), it experiences a phase transition at a specific noise level (Fig.23 A,B, E, F,H,I), aligning with the dictionary-learning literature (Studer & Baraniuk, 2012). In this noise experiment, CREIMBO further identifies that within-area ensemble composition correlations (Fig.23C,D) remain stable until a noise level of around $\sigma_{\text{noise}} \approx 10$, after which these correlations weaken as noise increases, which may imply that high noise in data can obscure meaningful relationships between ensembles. Additionally, it identified that the dynamics' coefficients remain robust until $\sigma_{\text{noise}} \approx 1.8$, while exhibiting an increasing internal frequency as the noise increases, potentially to account for noise that does not follow dynamical rules (Fig. 23G, 25). This suggests that frequency of fast transitions in CREIMBO's $\boldsymbol{c}_{k,t}$ could indicate noise in the system that does not adhere to the underlying dynamics.

CREIMBO Discovers Regional Interactions Predictive of Task Variables: We tested CREIMBO's ability to infer task-related variables from mice whole-brain Neuropixels multi-session data during a memory-guided movement (data from Chen et al. (2024), Fig. 26, 27). CREIMBO identifies intra- and inter-area brain interactions via the sub-circuits (Sec. F, Fig. 29C,D), including cross-regional flows into or from key areas responsible for memory (from $\boldsymbol{f}_5$ and to $\boldsymbol{f}_8$ the hippocampus), planning (from frontal cortex, e.g. $\boldsymbol{f}_3$), and movement (from primary motor cortex, $\boldsymbol{f}_4$), which are needed for the task. Within-area sub-circuits (Fig. 29D) further showed within-area ensemble interactions (e.g., the basal ganglia in $\boldsymbol{f}_1$ and the secondary motor cortex in $\boldsymbol{f}_2$, $\boldsymbol{f}_7$, along with self-activation/inhibition of ensembles in other sub-circuits (e.g. $\boldsymbol{f}_4$). Moreover, CREIMBO's dynamic coefficients ($\boldsymbol{c}_{kt}$) captured task-related patterns across trials and sessions (Fig. 4A,B). When training a regularized logistic-regression model, we found that we could predict from CREIMBO's circuits activations ($\boldsymbol{c}_{kt}$) various task variables including outcome, early lick, and lick side far above chance levels (Fig. 4C-J, p-values $< 1 \times 10^{-10}$). Furthermore, CREIMBO's sub-circuit activations across different task periods highlight how specific multi-regional interactions capture different aspects of the task. For instance, towards the trial end (t_3 window), which includes the lick movement, c_7 shows increased importance (Fig. 4E). Notably, c_7 corresponds to the activity of the $\boldsymbol{f}_7$ sub-circuit that captures flows to the secondary motor cortex (Fig. 29C). Another example is c_8 (activity of sub-circuit $\boldsymbol{f}_8$ that includes flows into hippocampus 29C), which shows increased feature importance in the first time window t_0. This aligns with the potential involvement of memory-related processes required with the stimulus appearance. Thus CREIMBO demonstrates the ability to capture interpretable neural dynamics and predict task variables that reveal complex regional interactions. (see Sec. F for more detailed results).

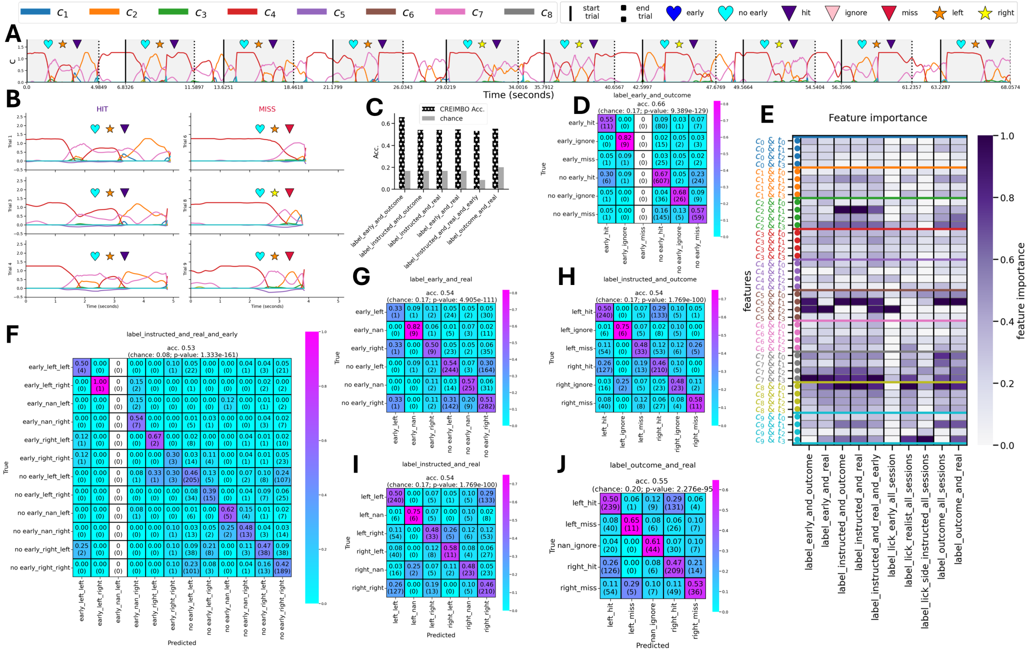

Figure 4: Results of task-variable prediction using CREIMBO's dynamic coefficients as input. Prediction was done based on coefficients from all used trials and sessions (19 sessions, 40-60 trials each, see Sec. F). **A:** Dynamic coefficients from example traces, shade marks within trial, bordered by starting and ending point. **B:** Dynamic coefficients for correct ("hit") vs. wrong ("miss") trials. **C:** Accuracy score of predicting task variables based on coefficients vs. chance. **D, F,G,H,I:** Confusion matrices of predicting varying task variables based on dynamic coefficients. **E:** importance of the different coefficients and time points for prediction.

5 DISCUSSION, LIMITATIONS, AND FUTURE WORK

Here, we introduced CREIMBO—a novel approach for uncovering multi-regional dynamics in neural data collected across multiple sessions. CREIMBO addresses the challenge of integrating non-simultaneous neural recordings by joint dynamical inference and sparsity regularization to capture the underlying neural sub-circuits governing brain activity. We further demonstrated the efficacy of CREIMBO through multiple synthetic and neural data, and found that CREIMBO recovered ground truth components and is robust to noise in identifying cross-regional motifs that span cross-session interactions. CREIMBO offers several advantages over existing methods. Chiefly, it identifies a cross-session shared latent space where non-stationary ensemble interactions are governed by a time-varying decomposition of universal basis dynamics. By structuring these dynamics in terms of global sub-circuits, CREIMBO allows the discovery of sub-circuits meaningful for various cognitive processes, enabling the identification of variability in neural activity across subjects and sessions.

Limitations & Future Directions: An important feature of CREIMBO is its ability to unify sessions with different neuron subsets through the universal dictionary of dynamical interactions prior that aligns ensembles in terms of functionality. This can enable the inference of their activity even if they are not observed in some sessions. This ability, however, depends on the overlap between the used basis interactions across sessions, the distinctiveness of different $\boldsymbol{f}_k$s, and the premise that the basis interactions capturing interactions with ensembles missing from a session include dynamic values for ensembles observed in that same session (Sec. D). Another limitation is CREIMBO's reliance on linear projections from ensemble to session observation space, restricting flexibility. Extending to non-linear projections offers potential for development, though it introduces computational and interpretability challenges. Finally, CREIMBO uses dictionary learning, which is computationally demanding, and future iterations will include parallel processing. Extending CREIMBO to additional data types and applications, including non-neural data (e.g., immune-cell counts), or for identifying pathological states is an exciting future direction.

REFERENCES

Kathryne M Allen, Angeles Salles, Sangwook Park, Mounya Elhilali, and Cynthia F Moss. Effect of background clutter on neural discrimination in the bat auditory midbrain. *Journal of neurophysiology*, 126(5):1772–1782, 2021.

Mikio Aoi and Jonathan W Pillow. Model-based targeted dimensionality reduction for neuronal population data. *Advances in Neural Information Processing Systems*, 31, 2018.

William E Bishop. *Combining Neural Population Recordings: Theory and Application.* PhD thesis, Carnegie Mellon University, USA, 2015.

William E Bishop and Byron M Yu. Deterministic symmetric positive semidefinite matrix completion. *Advances in Neural Information Processing Systems*, 27, 2014.

Po-Hsuan (Cameron) Chen, Janice Chen, Yaara Yeshurun, Uri Hasson, James Haxby, and Peter J Ramadge. A reduced-dimension fmri shared response model. In C. Cortes, N. Lawrence, D. Lee, M. Sugiyama, and R. Garnett (eds.), *Advances in Neural Information Processing Systems*, volume 28. Curran Associates, Inc., 2015.

Susu Chen, Thinh Nguyen, Nuo Li, and Karel Svoboda. Mesoscale activity map dataset (version 0.231012.2129), 2023. URL `https://doi.org/10.48324/dandi.000363/0.231012.2129`. [Data set].

Susu Chen, Yi Liu, Ziyue Aiden Wang, Jennifer Colonell, Liu D Liu, Han Hou, Nai-Wen Tien, Tim Wang, Timothy Harris, Shaul Druckmann, et al. Brain-wide neural activity underlying memory-guided movement. *Cell*, 187(3):676–691, 2024.

Mark M Churchland, John P Cunningham, Matthew T Kaufman, Justin D Foster, Paul Nuyujukian, Stephen I Ryu, and Krishna V Shenoy. Neural population dynamics during reaching. *Nature*, 487 (7405):51–56, 2012.

David F Crouse. On implementing 2d rectangular assignment algorithms. *IEEE Transactions on Aerospace and Electronic Systems*, 52(4):1679–1696, 2016.

Juan A Gallego, Matthew G Perich, Raeed H Chowdhury, Sara A Solla, and Lee E Miller. Long-term stability of cortical population dynamics underlying consistent behavior. *Nature neuroscience*, 23 (2):260–270, 2020.

Joshua Glaser, Matthew Whiteway, John P Cunningham, Liam Paninski, and Scott Linderman. Recurrent switching dynamical systems models for multiple interacting neural populations. *Advances in neural information processing systems*, 33:14867–14878, 2020.

Evren Gokcen, Anna I Jasper, João D Semedo, Amin Zandvakili, Adam Kohn, Christian K Machens, and Byron M Yu. Disentangling the flow of signals between populations of neurons. *Nature Computational Science*, 2(8):512–525, 2022.

Evren Gokcen, Anna Jasper, Alison Xu, Adam Kohn, Christian K Machens, and Byron M Yu. Uncovering motifs of concurrent signaling across multiple neuronal populations. *Advances in Neural Information Processing Systems*, 36, 2024.

Lukas Grossberger, Francesco P Battaglia, and Martin Vinck. Unsupervised clustering of temporal patterns in high-dimensional neuronal ensembles using a novel dissimilarity measure. *PLoS computational biology*, 14(7):e1006283, 2018.

Z. T. Harmany, R. F. Marcia, and R. M. Willett. This is spiral-tap: Sparse poisson intensity reconstruction algorithms – theory and practice. *IEEE Transactions on Image Processing*, 21: 1084–1096, Mar 2012.

Richard A Harshman. Foundations of the parafac procedure: Models and conditions for an "explanatory" multimodal factor analysis. *UCLA Working Papers in Phonetics*, 16(1):1–84, 1970.

Orren Karniol-Tambour, David M. Zoltowski, E. Mika Diamanti, Lucas Pinto, Carlos D Brody, David W. Tank, and Jonathan W. Pillow. Modeling state-dependent communication between brain regions with switching nonlinear dynamical systems. In *The Twelfth International Conference on Learning Representations*, 2024. URL `https://openreview.net/forum?id=WQwV7Y8qwa`.

Mohammad Reza Keshtkaran, Andrew R. Sedler, Raeed H. Chowdhury, Raghav Tandon, Diya Basrai, Sarah L. Nguyen, Hansem Sohn, Mehrdad Jazayeri, Lee E. Miller, and Chethan Pandarinath. A large-scale neural network training framework for generalized estimation of single-trial population dynamics. *bioRxiv*, 2021. doi: 10.1101/2021.01.13.426570. URL `https://www.biorxiv.org/content/early/2021/01/15/2021.01.13.426570`.

Michael Kyzar, Jan Kamiński, Aneta Brzezicka, Chrystal M Reed, Jeffrey M Chung, Adam N Mamelak, and Ueli Rutishauser. Dataset of human-single neuron activity during a sternberg working memory task. *Scientific Data*, 11(1):89, 2024.

Chengrui Li, Soon Ho Kim, Chris Rodgers, Hannah Choi, and Anqi Wu. One-hot generalized linear model for switching brain state discovery. In *The Twelfth International Conference on Learning Representations*, 2024. URL `https://openreview.net/forum?id=MREQ0k6qvD`.

Scott Linderman, Matthew Johnson, Andrew Miller, Ryan Adams, David Blei, and Liam Paninski. Bayesian learning and inference in recurrent switching linear dynamical systems. In *Artificial Intelligence and Statistics*, pp. 914–922. PMLR, 2017.

Scott Linderman, Benjamin Antin, David Zoltowski, and Joshua Glaser. SSM: Bayesian Learning and Inference for State Space Models (version 0.0.1, 10 2020. URL `https://github.com/lindermanlab/ssm`.

Scott W Linderman, Andrew C Miller, Ryan P Adams, David M Blei, Liam Paninski, and Matthew J Johnson. Recurrent switching linear dynamical systems. *arXiv preprint arXiv:1610.08466*, 2016.

Noga Mudrik, Yenho Chen, Eva Yezerets, Christopher J Rozell, and Adam S Charles. Decomposed linear dynamical systems (dlds) for learning the latent components of neural dynamics. *Journal of Machine Learning Research*, 25(59):1–44, 2024a.

Noga Mudrik, Gal Mishne, and Adam Shabti Charles. Sibblings: Similarity-driven building-block inference using graphs across states. In *Forty-first International Conference on Machine Learning*, 2024b.

Noga Mudrik, Eva Yezerets, Yenho Chen, Christopher Rozell, and Adam Charles. Linocs: Lookahead inference of networked operators for continuous stability. *arXiv preprint arXiv:2404.18267*, 2024c.

K. P. Murphy. Switching Kalman filters. Technical report, Technical Report, UC Berkeley, 1998.

Marcel Nonnenmacher, Srinivas C Turaga, and Jakob H Macke. Extracting low-dimensional dynamics from multiple large-scale neural population recordings by learning to predict correlations. *Advances in neural information processing systems*, 30, 2017.

Chethan Pandarinath, Daniel J. O'Shea, Jasmine Collins, Rafal Jozefowicz, Sergey D. Stavisky, Jonathan C. Kao, Eric M. Trautmann, Matthew T. Kaufman, Stephen I. Ryu, Leigh R. Hochberg, and et al. Inferring single-trial neural population dynamics using sequential auto-encoders. *Nature Methods*, 15:805–815, Sep 2018. doi: 10.1038/s41592-018-0109-9.

Bijan Pesaran, Maureen Hagan, Shaoyu Qiao, and Ryan Shewcraft. Multiregional communication and the channel modulation hypothesis. *Current opinion in neurobiology*, 66:250–257, 2021.

Kaare Brandt Petersen, Michael Syskind Pedersen, et al. The matrix cookbook. *Technical University of Denmark*, 7(15):510, 2008.

Steffen Schneider, Jin Hwa Lee, and Mackenzie Weygandt Mathis. Learnable latent embeddings for joint behavioural and neural analysis. *Nature*, May 2023. ISSN 1476-4687. doi: 10.1038/s41586-023-06031-6. URL `https://doi.org/10.1038/s41586-023-06031-6`.

João D Semedo, Amin Zandvakili, Christian K Machens, M Yu Byron, and Adam Kohn. Cortical areas interact through a communication subspace. *Neuron*, 102(1):249–259, 2019.

Max Simchowitz, Horia Mania, Stephen Tu, Michael I Jordan, and Benjamin Recht. Learning without mixing: Towards a sharp analysis of linear system identification. In *Conference On Learning Theory*, pp. 439–473. PMLR, 2018.

Daniel Soudry, Suraj Keshri, Patrick Stinson, Min-hwan Oh, Garud Iyengar, and Liam Paninski. A shotgun sampling solution for the common input problem in neural connectivity inference. *arXiv preprint arXiv:1309.3724*, 2013.

Christoph Studer and Richard G Baraniuk. Dictionary learning from sparsely corrupted or compressed signals. In *2012 IEEE International Conference on Acoustics, Speech and Signal Processing (ICASSP)*, pp. 3341–3344. IEEE, 2012.

Aneel Tanwani, Hyungbo Shim, and Daniel Liberzon. Observability for switched linear systems: characterization and observer design. *IEEE Transactions on Automatic Control*, 58(4):891–904, 2012.

Srini Turaga, Lars Buesing, Adam M Packer, Henry Dalgleish, Noah Pettit, Michael Hausser, and Jakob H Macke. Inferring neural population dynamics from multiple partial recordings of the same neural circuit. *Advances in Neural Information Processing Systems*, 26, 2013.

Jacob L Yates, Il Memming Park, Leor N Katz, Jonathan W Pillow, and Alexander C Huk. Functional dissection of signal and noise in mt and lip during decision-making. *Nature neuroscience*, 20(9): 1285–1292, 2017.

Feng Zhu, Harrison A Grier, Raghav Tandon, Changjia Cai, Anjali Agarwal, Andrea Giovannucci, Matthew T Kaufman, and Chethan Pandarinath. A deep learning framework for inference of single-trial neural population dynamics from calcium imaging with subframe temporal resolution. *Nature neuroscience*, 25(12):1724–1734, 2022.

Hui Zou, Trevor Hastie, and Robert Tibshirani. Sparse principal component analysis. *Journal of computational and graphical statistics*, 15(2):265–286, 2006.

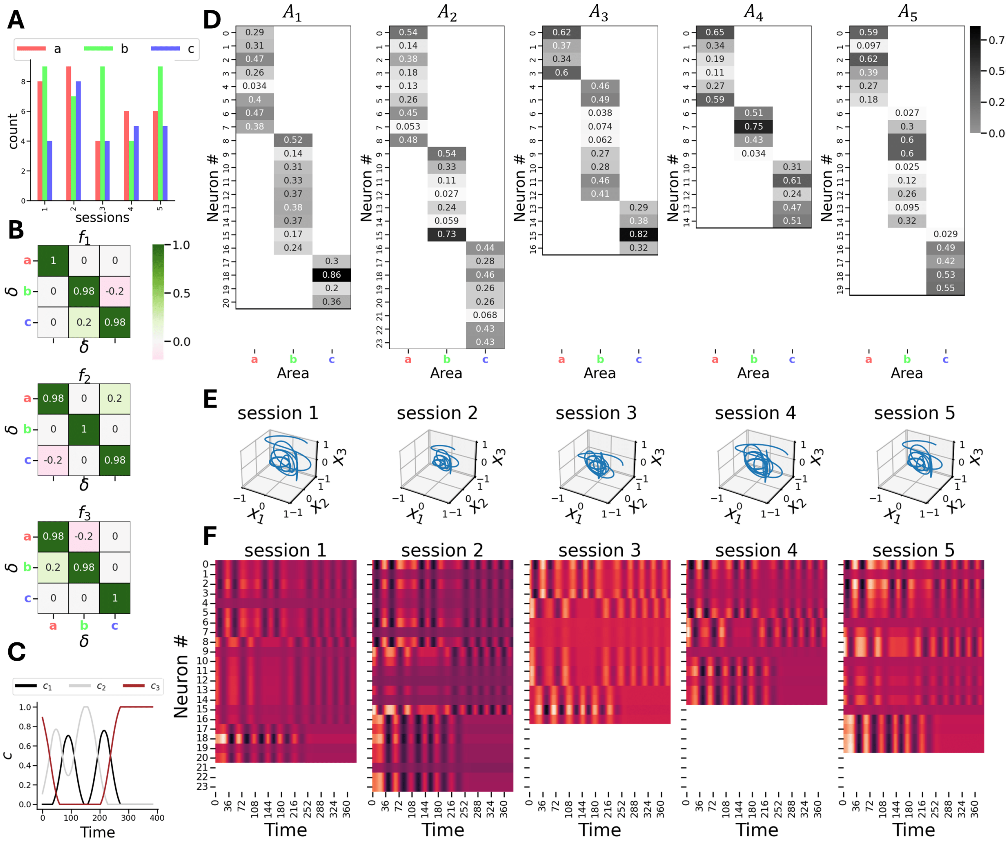

Figure 5: **A:** Distribution of neurons across areas (areas a, b, and c) over the 5 different synthetic sessions. **B:** Ground truth sub-circuits are $K = 3$ rotational matrices, each captures a different rotational direction. **C:** Time-coefficients of synthetic sub-circuits. **D:** Synthetic ensembles ($\{\boldsymbol{A}^d\}_{d=1}^5$ **E:** Latent (ensemble) dynamics. Different trajectories in the latent space emerge as distinct cross-session time-changing decomposition of the ensemble sub-circuits. **F:** Synthetic Ground Truth observations ($\{\boldsymbol{Y}_d\}$)

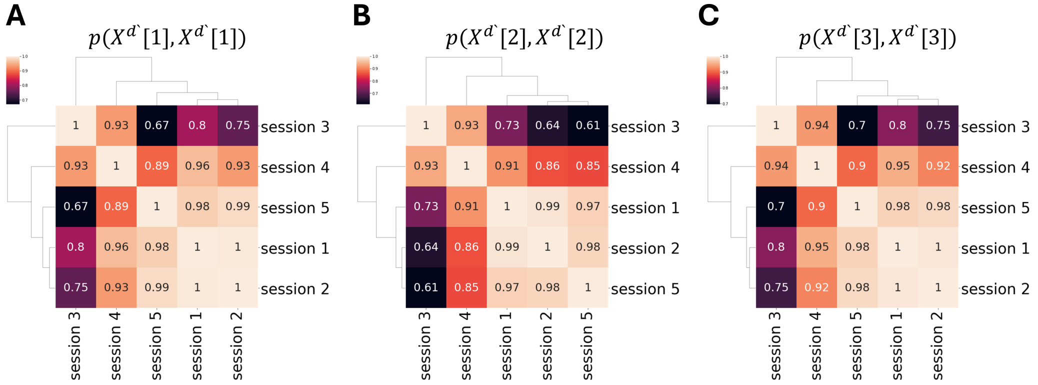

Figure 6: Clustermaps of correlations of cross-session latent dynamics. Each subplot captures one dimension of the latent dynamics.

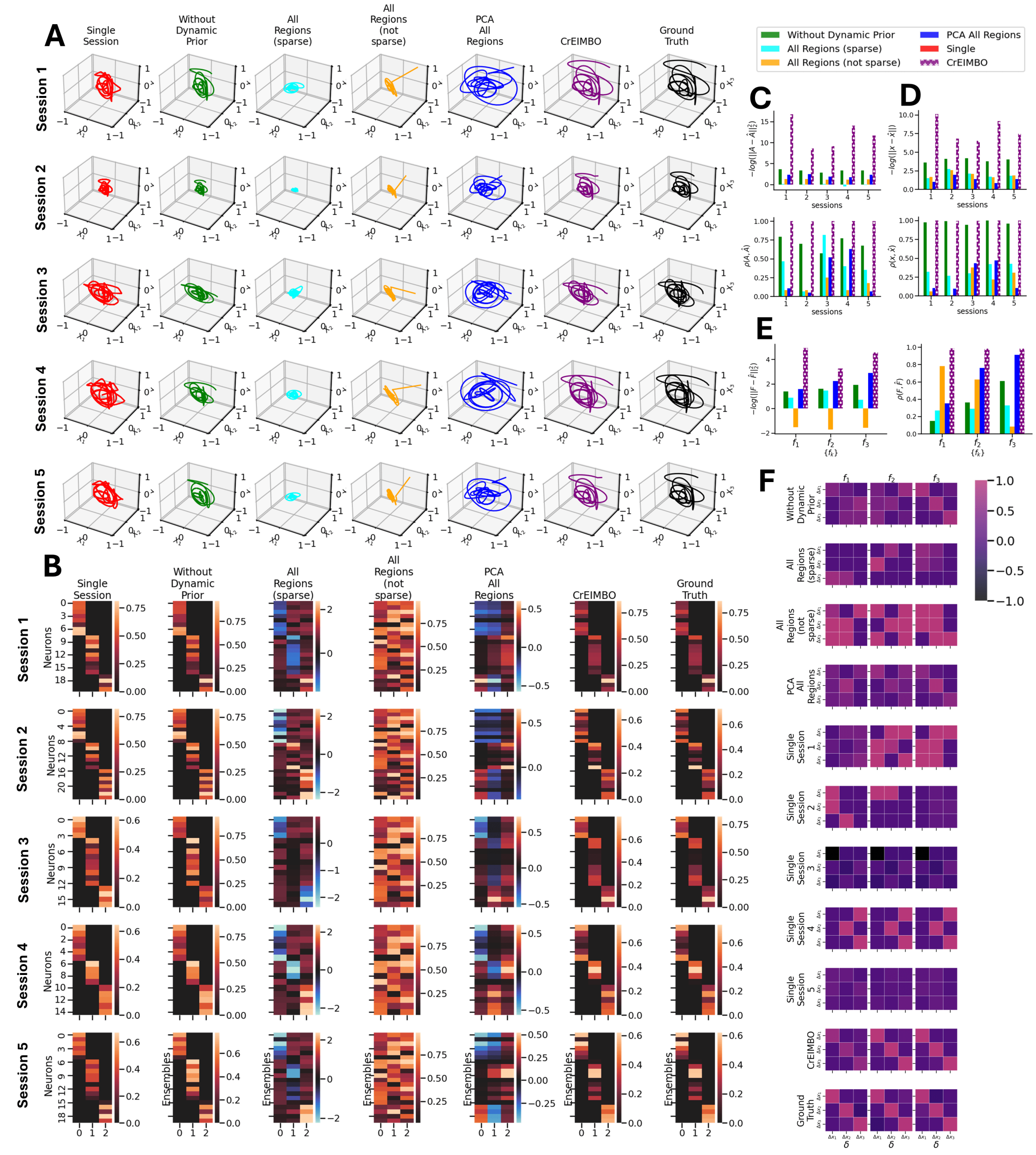

Figure 7: Comparison between CREIMBO to the baselines reveal that CREIMBO outperforms other approaches (see baselines details in Sec. D). **A:** Learned latent dynamics ($\boldsymbol{X}$) for each of the 5 sessions (rows) for the different methods (columns). **B:** Learnt ensemble compositions ($\boldsymbol{A}$) for each of the 5 sessions (rows) for the different methods (columns). **C-E:** $-log(MSE)$ and correlation between the ground truth and the the identified ensemble compositions (in **C**), latent dynamics (in **D**), and sub-circuits (in **E**). **F:** Heatmaps of the identified sub-circuits for the different methods.

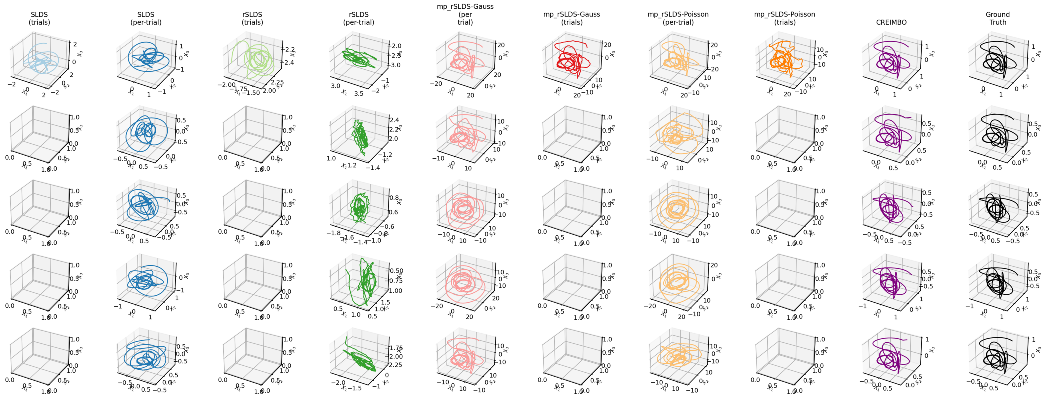

Figure 8: Further comparisons of the learned latent dynamics to these learned by SLDS, rSLDS, and multi-region rSLDS, with their variations (see Sec. D for details). Different columns represent different methods. Different rows capture different sessions.

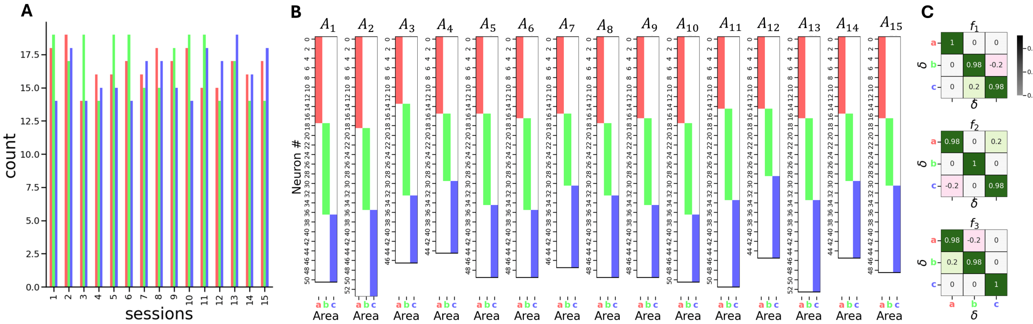

Figure 9: Distribution of areas in second synthetic dataset. **A:** Histogram of neural counts per area and session. **B:** Ensemble masks ($\boldsymbol{A}_{\text{mask}}$) across sessions. **C:** Ground truth sub-circuits.

Algorithm 1 CREIMBO training

```
Input: $p, K, \sigma_h, \beta_1, \beta_2, \beta_3, \lambda_x, \lambda_c, \lambda_f, \lambda_\rho, \lambda_{\text{obs}}$, Batch Size
Initialize: $\{f_k\}_{k=1}^K$, $\{c_d\}_{d=1}^D$, $\{x_d\}_{d=1}^D$
Pre-calculate: $\{h_j\}_{j=1}^J$
repeat
    for each session $d$ in a random batch of $D$ do
        Update ensembles
        Update hidden dynamics and coefficients
    Select a random batch of sessions from $D$
    Update networks $\{f_k\}$
    if stuck in local minimum then
        Perturb $\{f_k, c_d\}$
until convergence
```

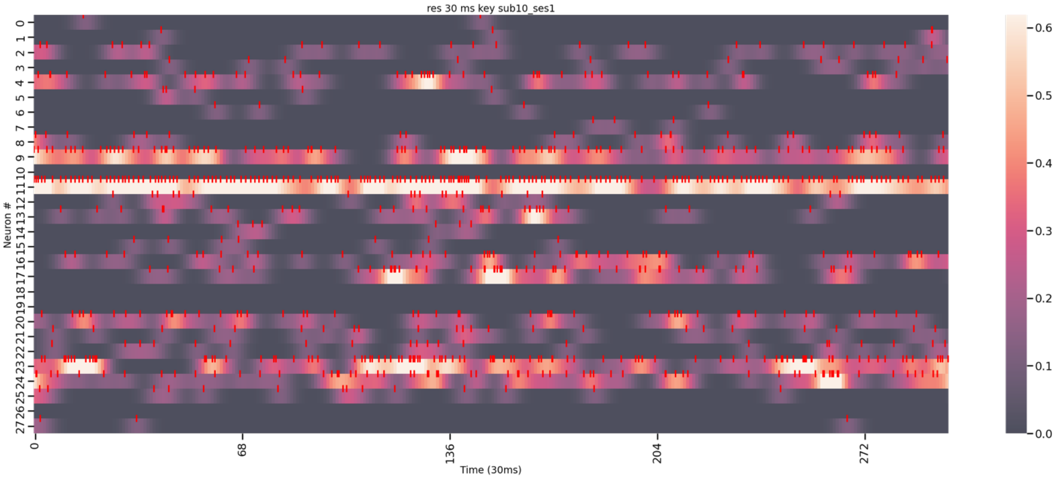

Figure 10: Rate estimation example for a specific session using a 30 ms Gaussian kernel.

A NOTATIONS

Symbol	**Description**
D	Number of sessions (encompassing both same and different subjects)
M_d	Number of trials for each session d
$\boldsymbol{Y}_m^d$	Neural recordings firing rate estimation for trial m and session d
N_m^d	Number of neurons observed in trial m of session d
T_m^d	Number of time points observed in trial m of session d
$\{\boldsymbol{Y}_m^d\}_{m,d}$	Overall set of observations
$\boldsymbol{A}_m^d$	The neuronal composition of each sparse ensemble in trial m and session d
$\boldsymbol{A}_{\text{block}}$	Block of $\boldsymbol{A}$ representing neural dynamics in a specific brain area
n_j	Total neurons in area j
p_j	Maximum number of ensembles discernible within area j
p	Total number of ensembles across all areas
J	Total number of distinct brain areas
n	Total neurons involved across all trials or sessions
$\boldsymbol{x}_t$	State vector at time t
$\boldsymbol{F}_t$	Transition matrix at time t, representing ensemble interactions
K	Number of global interacting units
$\boldsymbol{c}_{kt}$	Influence of the k-th global interaction at time t
$\boldsymbol{f}_k$	Basic linear system representing the k-th global interaction
$\tau = \mathrm{T}_m^d$	Duration of the trial or session

B PARAMETERS RANGE FOR SYNTHETIC DATA EXPERIMENT

The full set of parameters for the synthetic experiments are available in Table 1.

C PARAMETERS FOR HUMAN MULTI-REGIONAL EXPERIMENT

The full set of parameters for the human data experiment are available in Table 2.

D INFORMATION ABOUT THE BASELINES:

We distinguish between two types of baselines: (1) ablation experiments and (2) comparison to the performance of entirely different methods. It is important to note that the latter cannot fully capture the unique capabilities of CREIMBO, particularly in identifying basis ensemble interactions shared

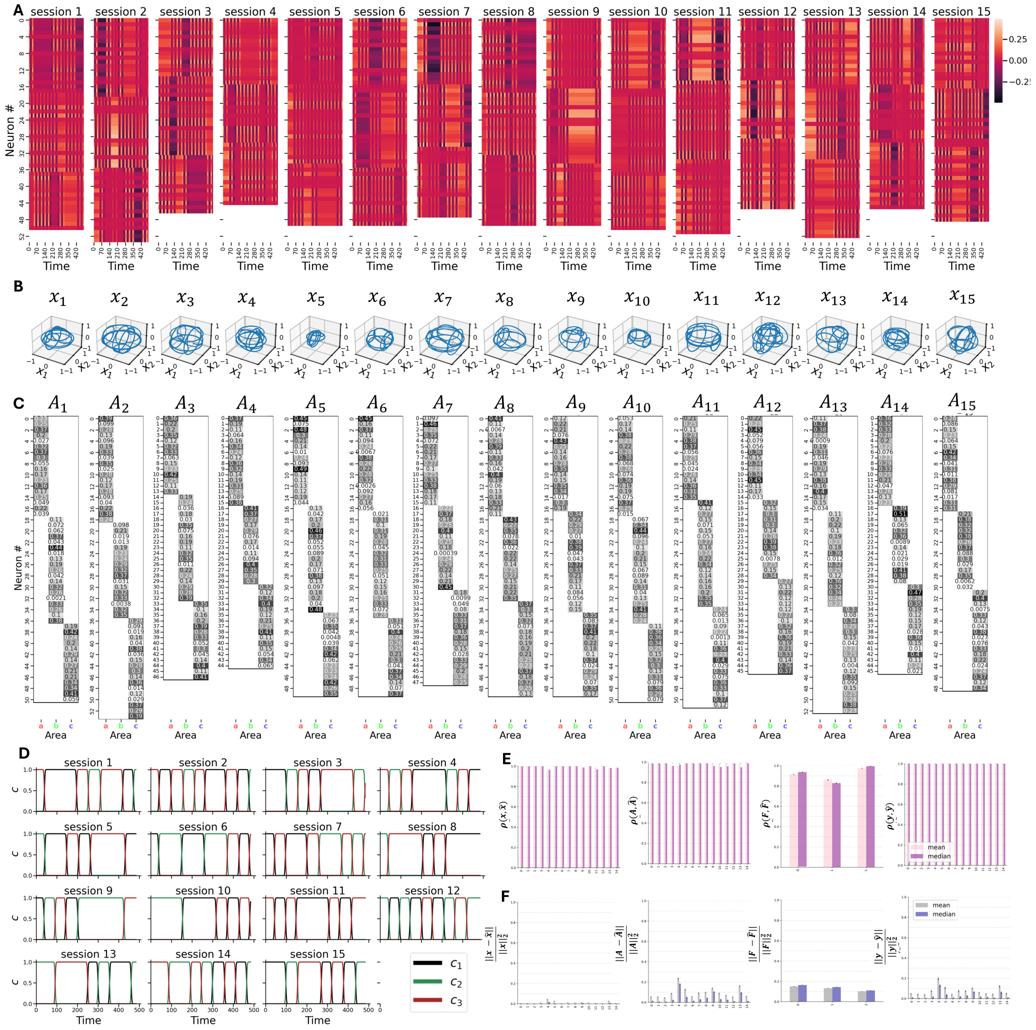

Figure 11: Data and results for the second synthetic experiment (overall $D = 15$ sessions, $J = 3$ regions and $p_j = 1$ ensembles for each region $j = 1 \ldots J$). **A:** Ground truth synthetic observations. **B:** Ground truth latent dynamics ($\{\boldsymbol{X}^d\}_{d=1}^{D=15}$). **C:** Ground truth ensemble compositions ($\{\boldsymbol{A}^d\}_{d=1}^{D=15}$). **D:** Ground truth sub-circuits coefficients (c) vary between sessions. **E:** Correlation between ground truth and identified components for **A** (left), **x** (middle left), **F** (middle right), **Y** (right). **F:** ℓ_2 distance between the components learned by CREIMBO and the ground-truth components for **A** (left), **x** (middle left), **F** (middle right), **Y** (right).

across sessions through sparse decomposition. Therefore, we only compare certain aspects that can be extracted from other methods (e.g., multi-regional SLDS, which requires the same number of neurons per session). However, these comparisons do not imply that other models outperform or underperform CREIMBO; they simply offer different insights, with varying strengths and limitations depending on the application.

Importantly, since the sub-circuits $\{\boldsymbol{f}_k\}$ is invariant to its ordering, we used SciPy's implementation of the 'linear_sum_assignment' problem Crouse (2016) to re-order the identified sub-circuits before comparing them with the ground truth, matching the $\boldsymbol{f}$s values by minimizing the ℓ_2 error. **Ablation Experiments:**

1. "**Without Dynamic Prior**": Running CREIMBO while removing the prior over the dynamics from the inference. Instead, inferring the temporal traces of the ensembles using

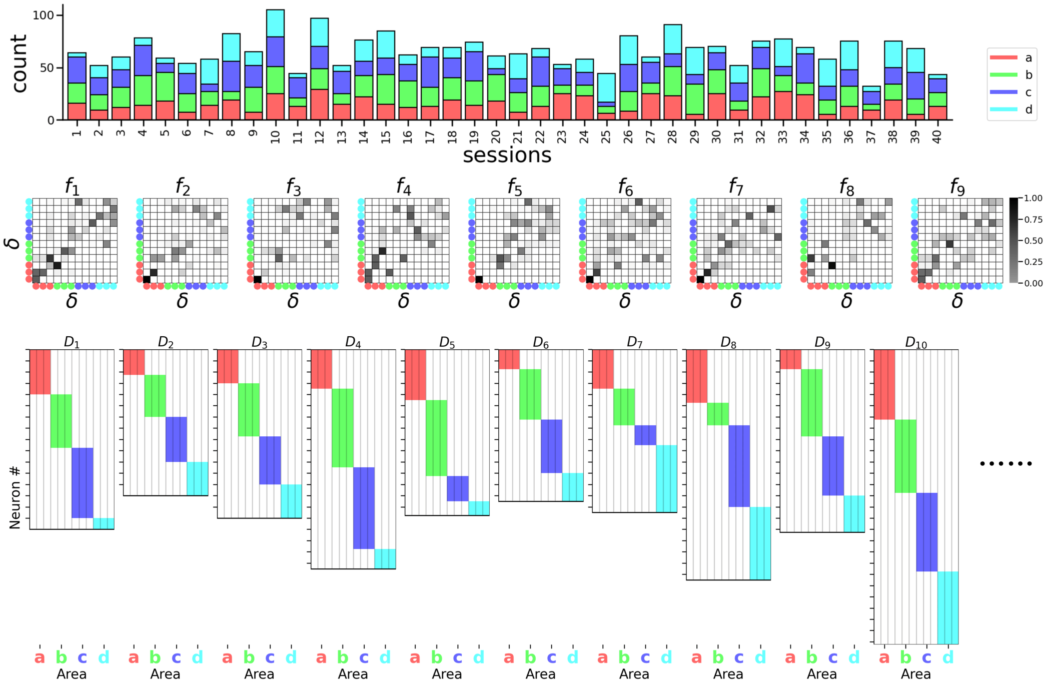

Figure 12: Multi-ensemble synthetic data. Top: Distribution of areas across sessions. Middle: Ground truth sub-circuits. Bottom: Masks for ensembles identification.

regularized least-squares with the addition of smoothness, de-correlation, and Frobenius norm regularization terms on the dynamics.

2. "**All Regions (sparse)**": Running CREIMBO without applying the multi-regional diagonal mask over the ensemble compositions ($\boldsymbol{A}$), thus supporting the finding of non-localized ensembles.
3. "**All Regions (non-sparse)**": Similar to the previous one but without applying sparsity on the ensemble matrix.
4. "**PCA All Regions**": Running CREIMBO while replacing the dimensionality reduction step with PCA.
5. "**Single Session #**": Running CREIMBO on a single session (view) of the data rather than leveraging cross-session information.

Other methods:

1. "**SLDS**": We used the SSM Python package described by Linderman et al. at Linderman et al. (2020). For the (non-recurrent) SLDS option, we used the "gaussian_orthog" emission parameter, the "bbvi" as the fitting method, "variational_posterior" was set to "mf", and the number of iterations ("num_iters") was set to 500. The rest of the fitting parameters were left as default. We were inspired by this notebook `https://github.com/lindermanlab/ssm/blob/master/notebooks/3-Switching-Linear-Dynamical-System.ipynb` by Linderman et al. (2020) for our comparison. This includes:
   1) "**SLDS (trials)**" which captures the training of SLDS with "bbvi" fitting method from across all trials (by stacking trials information vertically),
   2) "**SLDS (per-trial)**" which refers to training SLDS individually per-trial.
2. "**rSLDS**": Similarly to SLDS, for the recurrent version (rSLDS, (Linderman et al., 2016)), we used the same SSM package provided by Linderman et al. (2020). Here, we used the recurrent option for the transitions (i.e., the "transitions" parameter was set to"recurrent_only"), using "diagonal_gaussian" dynamics and "gaussian_orthog" emissions. This includes:

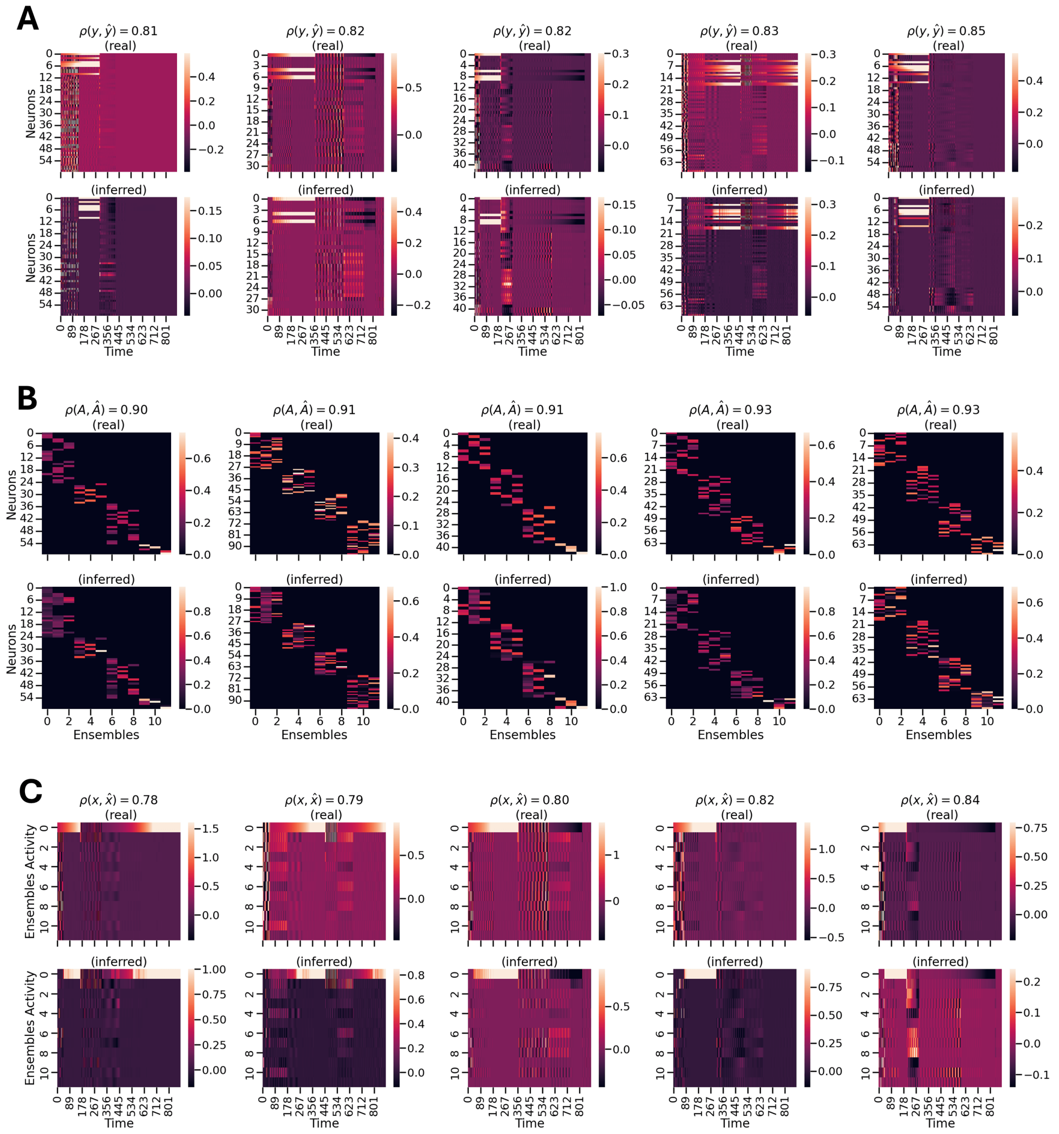

Figure 13: Multi-ensemble synthetic data results. Top: Recovering the observations $\boldsymbol{Y}$ (five exemplary sessions). Middle: Identified Ensembles (five exemplary sessions). Bottom: Identified latent dynamics (five exemplary sessions).

3) “**rSLDS (trials)**” which captures training rSLDS with the “bbvi” fitting method from across all trials (by stacking trials information vertically),
4) “**rSLDS (per-trial)**” which refers to training rSLDS individually per-trial.

3. **“mp_rSLDS”**: Multi-Regional rSLDS, as described in Glaser et al. (2020). To run our comparison, we were inspired by the colab-notebook for this “mp_rslds” method, provided by the SSM Python Package Linderman et al. (2020) (at `https://colab.research.google.com/github/lindermanlab/ssm/blob/master/notebooks/Multi-Population-rSLDS.ipynb`). This includes:
5) “**mp_rSLDS-Gauss (trials)**” which captures training “mp_rSLDS” from across all trials (by stacking trials information vertically) under Gaussian statistics.
6) “**mp_rSLDS-Gauss (per-trial)**” which refers to training “mp_rSLDS” individually per-trial under Gaussian statistics.
7) “**mp_rSLDS-Poisson (trials)**” which captures training “mp_rSLDS” with the “bbvi”

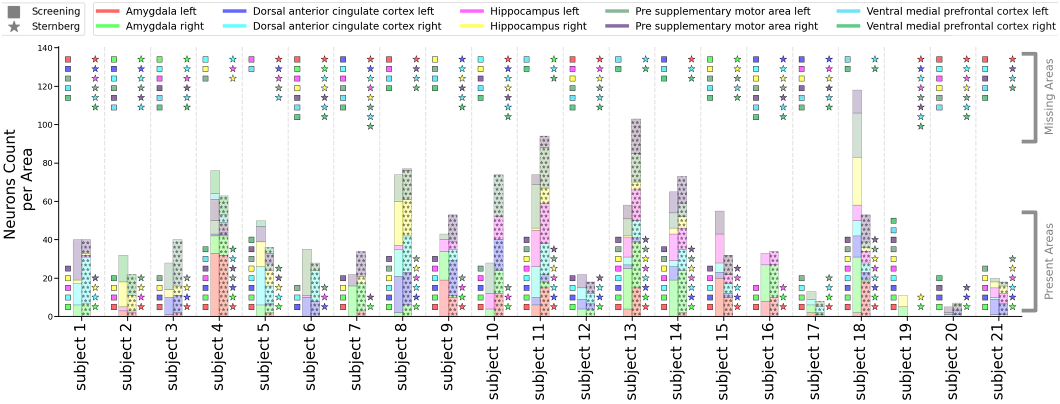

Figure 14: Areas distribution in real world human neural data.

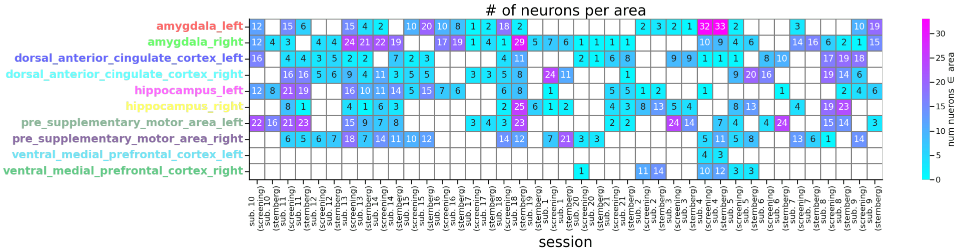

	sub. 10 (screening)	sub. 10 (sternberg)	sub. 11 (screening)	sub. 11 (sternberg)	sub. 12 (screening)	sub. 12 (sternberg)	sub. 13 (screening)	sub. 13 (sternberg)	sub. 14 (screening)	sub. 14 (sternberg)	sub. 15 (screening)	sub. 15 (sternberg)	sub. 16 (screening)	sub. 16 (sternberg)	sub. 17 (screening)	sub. 17 (sternberg)	sub. 18 (screening)	sub. 18 (sternberg)	sub. 19 (sternberg)	sub. 1 (screening)	sub. 1 (sternberg)	sub. 20 (screening)	sub. 20 (sternberg)	sub. 21 (screening)	sub. 21 (sternberg)	sub. 2 (screening)	sub. 2 (sternberg)	sub. 3 (screening)	sub. 3 (sternberg)	sub. 4 (screening)	sub. 4 (sternberg)	sub. 5 (screening)	sub. 5 (sternberg)	sub. 6 (screening)	sub. 6 (sternberg)	sub. 7 (screening)	sub. 7 (sternberg)	sub. 8 (screening)	sub. 8 (sternberg)	sub. 9 (screening)	sub. 9 (sternberg)
amygdala_left	12		15	6			15	4	2		10	20	10	8	1	2	18	2								2	3	2	1	32	33	2				3				10	19
amygdala_right	12	4	3		4	4	24	21	22	19			17	19	1	4	1	29	5	7	6	1	1	1	1					10	9	4	6			14	16	6	2	1	15
dorsal_anterior_cingulate_cortex_left	16		4	4	3	5	2	2		7	2	3					4	11				2	1	6	8			9	9	1	1	1		8	10			17	19	18	
dorsal_anterior_cingulate_cortex_right			16	16	5	6	9	4	11	3	5	5			3	3	5	8		24	11				1							9	20	16				19	14	6	
hippocampus_left	12	8	21	19			16	10	11	14	5	15	7	6			6	8		1				5	5	1	2			1					1				2	4	6
hippocampus_right			8	1			4	1	6	3							2	25	6	1	2			4	3	8	13	5	4			8	13			4		19	23		
pre_supplementary_motor_area_left	22	16	21	23			15	9	7	8					3	4	3	23						2	2			24	14		7	4		4	24			15	14		3
pre_supplementary_motor_area_right			6	5	6	7	18	7	14	11	10	12					14	12		7	21	3	3							5	11	5	8			13	6	1		14	
ventral_medial_prefrontal_cortex_left																														4	3										
ventral_medial_prefrontal_cortex_right																						1				11	14			10	12	3	3								

Figure 15: Number of neurons per-area and per-session in the real-world human data taken from Kyzar et al. (2024).

fitting method from across all trials (by stacking trials information vertically) under Poisson statistics.

8) “**mp_rSLDS-Poisson (per trial)**” which refers to training “mp_rSLDS” individually per-trial under Poisson statistics.

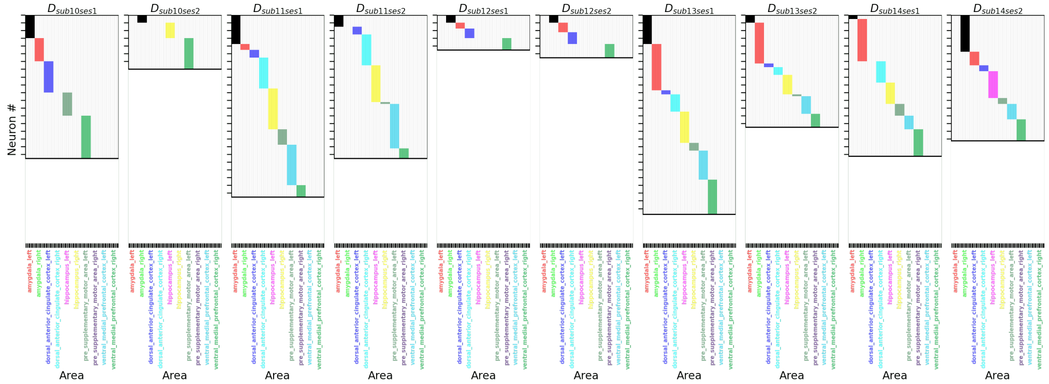

Figure 16: Multi-regional Masks for real-world human data.

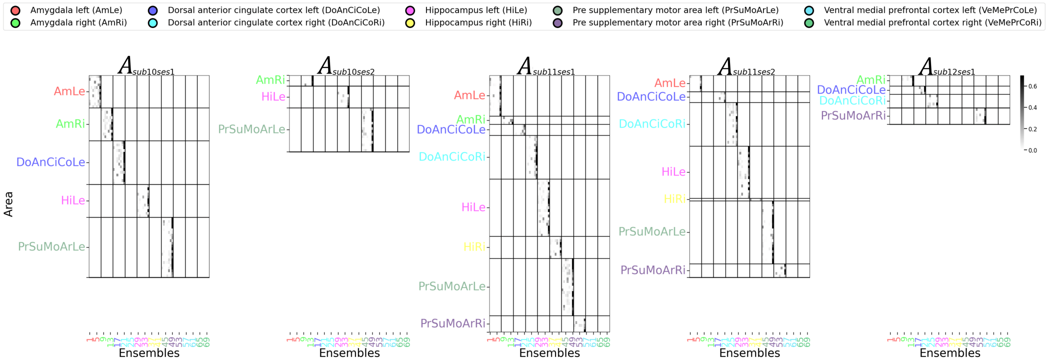

Figure 17: Five Exemplary Ensemble Matrices of the Real World Data, as Identified by CREIMBO

ASSUMPTIONS

The CREIMBO model is based on a core set of assumptions over the nature of the data. These assumptions draw on both known properties of neural processes and general well-known statistical models used widely in data science. We categorize these assumptions into two types:

1. Priors over the underlying neural processes.
2. Priors over Observational Constraints in order for CREIMBO to properly infer the underlying system by leveraging multi-session information.

D.1 PRIORS OVER THE UNDERLYING NEURAL PROCESSES

1. The neural dynamics in each session d are assumed to lie on a low-dimensional manifold, embedded in a $P << N^d$ low-dimensional space that is defined by P functional groups of neurons (referred to as “ensembles”).
2. We assume that these functional ensembles consist of neurons with co-activation patterns, where neurons can belong to more than one, but only *a few* (a sparse number) of ensembles, with varying degrees of membership.
3. We further propose that the interactions between these ensembles drive the evolution of the latent manifold over time and are key to encoding changes in conditions and behavior.
4. For CREIMBO to be effective, we assume these interactions arise from the joint synchronous activity of multiple co-occurring processes, captured by a limited-size set of “basis-ensemble-interactions”. The time-varying, sparse decomposition of these basis-ensemble-interactions, weighted by their time-local contributions in every time point, can adequately describe the manifold’s evolution over time.

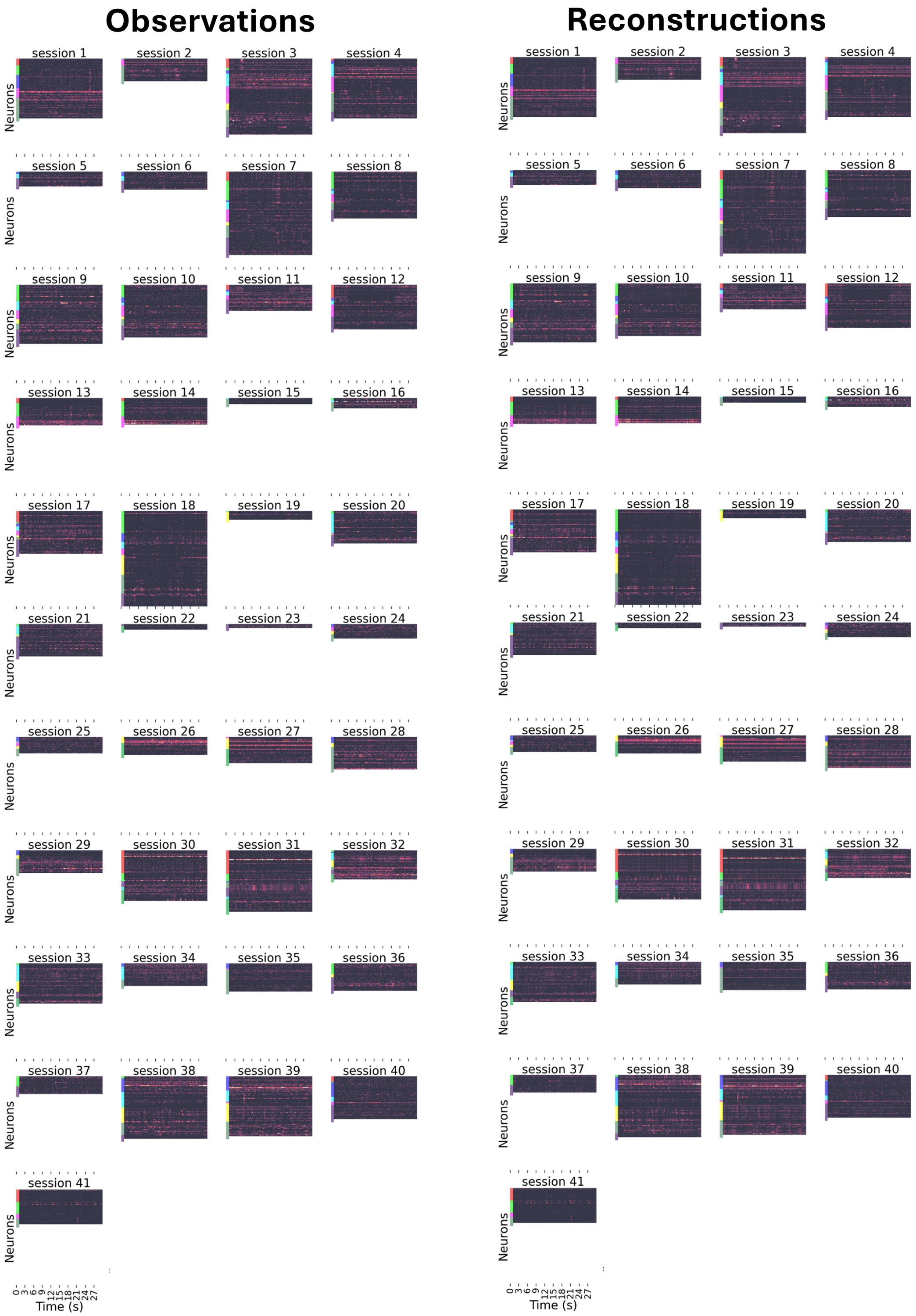

Figure 18: Observations vs. CREIMBO's reconstructions for the real-world human data experiment.

5. We assume that different dynamics basis elements capture distinct processes or behaviors. Some processes are required to be globally related to the cognitive task, while others capture session- or subject-specific processes (see Sec. D.2).

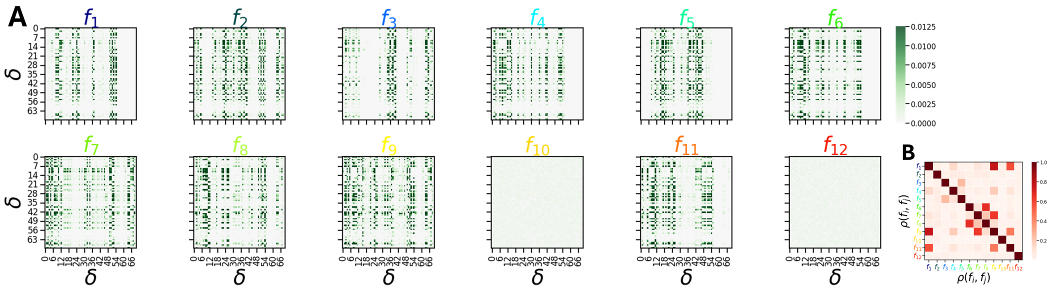

Figure 19: The sub-circuits underlying human data as identified by CREIMBO. **A**: The identified 12 sub-circuits. **B**: Pairwise correlations between the identified sub-circuits.

Table 1: Parameter values for synthetic experiments

Parameter	**Value (range)**	**Explanation**
same_c	False	Indicates if to use shared sub-circuits coefficients across sessions.
step_f	0.1 - 0.5	Gradient descent step size for updating $\boldsymbol{f}$
GD_decay	0.99 - 0.999	Decay over iterations of gradient-descent step size.
max_error	1e-09	The error threshold to stop training the model.
max_iter	500	Threshold on the maximum number of iterations.
include_D	True	Indicates the inclusion of a projection to a latent space.
step_D	$10^{-5} - 10^{-2}$	Range of Gradient Descent Step size for $\boldsymbol{A}$.
seed	0 - 4000	Random seed to choose from
normalize_eig	True , False	Indicates if to normalize the sub-circuits by
start_sparse_c	False , True	Whether to initialize c to be sparse.
sparse_f	True	Whether to apply sparsity on the sub-circuits
num_gradient_steps	1 -3	Number of gradient steps in an iteration.
add_avg	True , False	Whether to add a moving average to an iteration.
sparsity_on_f_max	40-60	Percentile of sparsity applied on each $\boldsymbol{f}$
take_multiple_gd	False, True	Indicates if to take multiple steps of gradient descent.
D_graph_driven	True	Indicates that D is inferred with graph-driven way.
infer_x_c_together	False , True	Indicates if the inference of $\boldsymbol{x}$ and $\boldsymbol{c}$ occurred simultaneously.
include_mask	True	Indicates the inclusion of a mask on $\boldsymbol{A}$
norm_D_cols	True	Indicates the normalization of columns of $\boldsymbol{A}$
lambda_D	0.1 - 0.3	Regularization weight on updating $\boldsymbol{A}$
step_D_decay	0.99 - 0.9999	Decay rate for updating $\boldsymbol{A}$ parameters
num_regions	3	Number of brain regions.
lambda_x	0 - 0.1	Sparsity term on the latent dynamics.
latent_dim	3	Latent dimension.
noise_level	0.2-0.6	Standard deviation of noise added to the data.
num_subdyns	3	Number of sub-circuits.
lasso_solver	'spgl1'	Pylops solver used for ℓ_1 regularization.

6. Each of these ensemble interactions may capture between-area interactions, within-area interactions, or both.

D.2 PRIORS OVER OBSERVATIONAL CONSTRAINTS

To effectively learn a unified representation by leveraging information across sessions, we make the following assumptions on the statistics of the data.

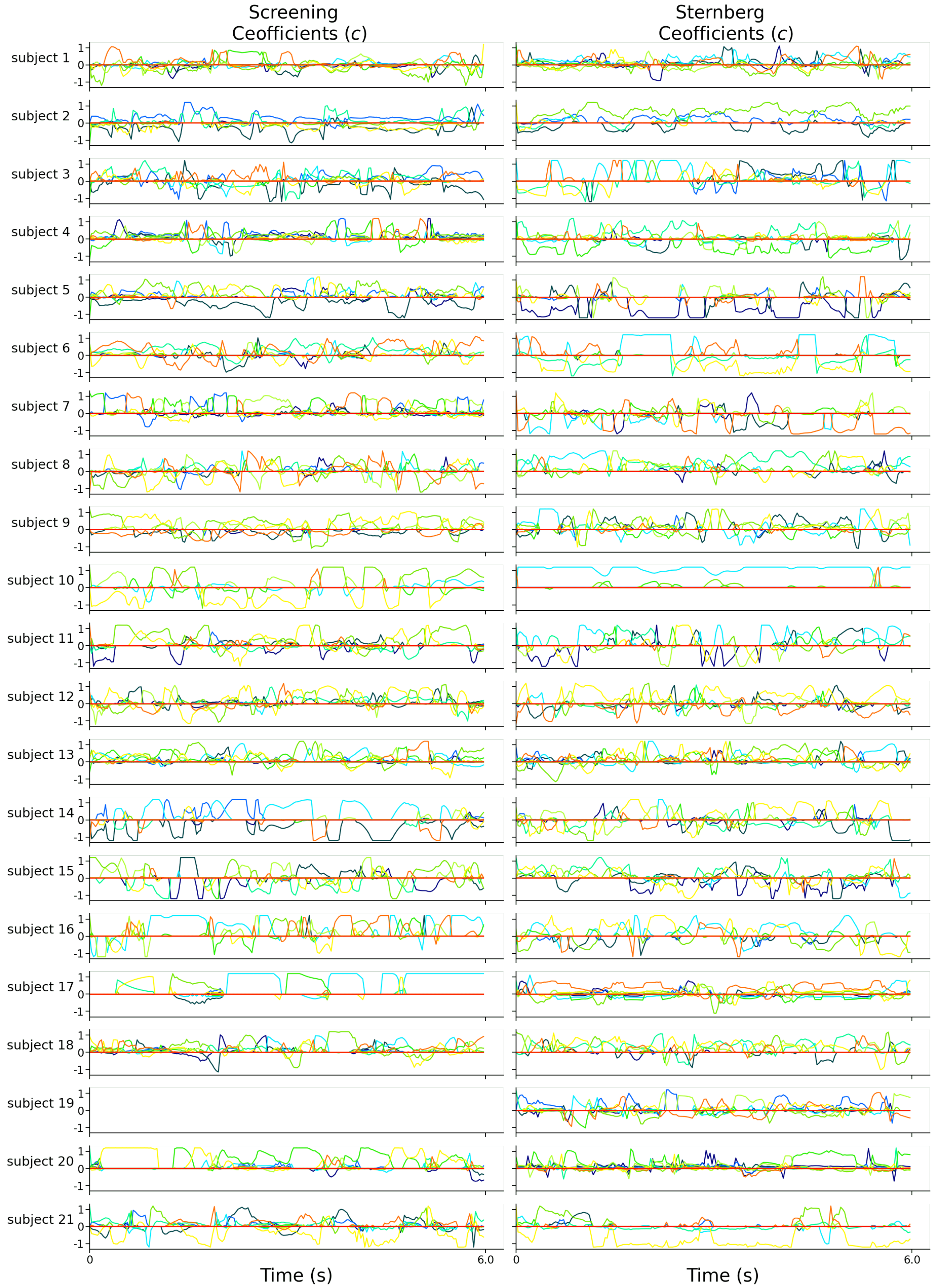

Figure 20: Sub-circuits Coefficients separated by task type ("Screening" vs "Sternberg") and subject.

1. Our ability to infer the underlying latent state (see Fig. 1B) is contingent upon the overall observability of the dynamical system. In traditional linear systems, the observability matrix can guarantee that any state is visible in a finite time horizon output. Non-stationary systems, as in CREIMBO, do not have succinct guarantees, the closest of which come in the form of observability conditions on switched linear systems (Tanwani et al., 2012).

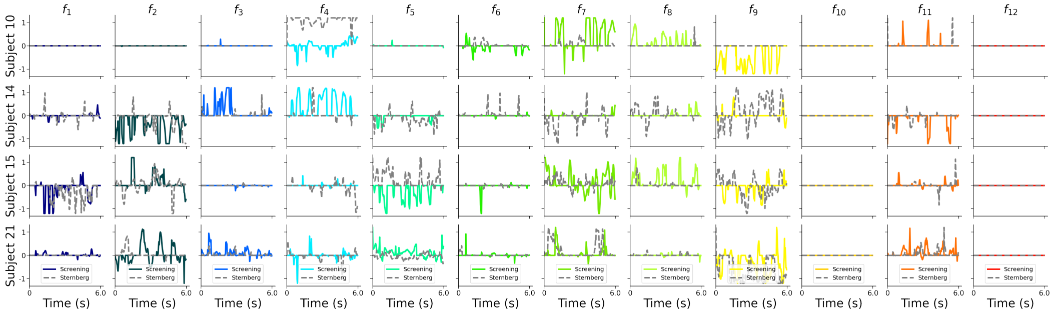

Figure 21: Comparing the use of the same coefficient under 'Sternberg' vs 'Screening' within four exemplary subject, reveals usage of similar sub-circuits within subjects.

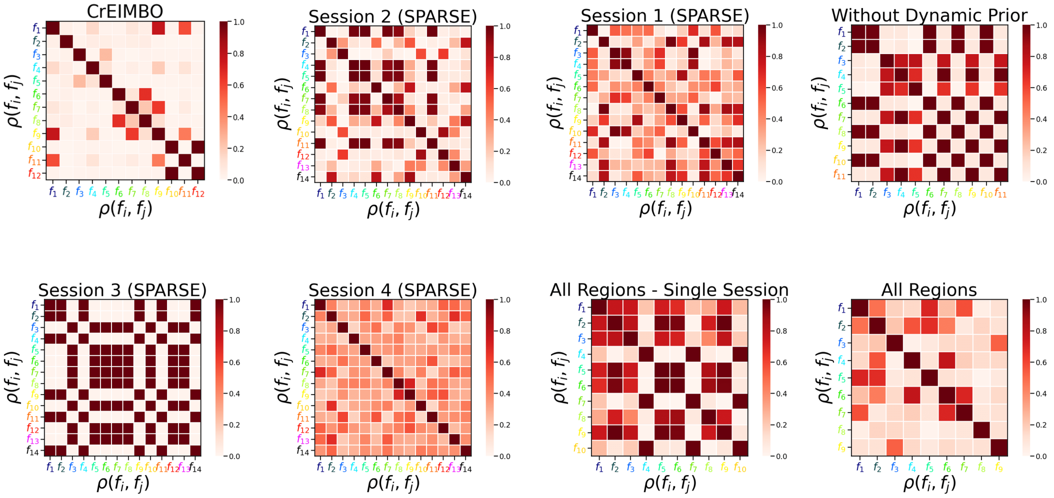

Figure 22: Correlations between the brain sub-circuits identified by CREIMBO compared to the other methods. These results highlight the CREIMBO discovers more distinct sub-circuits than these idetified by the other methods.

As the heart of the observability condition is that the dynamics "well mixes" the state such that any state element in the null space of the readout matrix will eventually be rotated into the its span, and thus visible. We thus assume that the spectral radius of each dynamical system (a measure of mixing in linear systems (Simchowitz et al., 2018)) in the basis is close to one. This assumption is loose, due to the lack of theoretical guarantees on general nonstationary systems, and further analysis should identify tighter, and less stringent, assumptions.

2. Another prior we want to consider is which $\boldsymbol{f}$s capture ensembles unobserved in certain sessions, allowing us to assert that CREIMBO can recover the activity of these unobserved ensembles during those sessions. To achieve this, we must ensure that in the sessions where these ensembles are unobserved, at least some $\boldsymbol{f}$s representing them also capture the activity of observed ensembles. For example, if certain missing ensembles are represented solely by $\boldsymbol{f}$s that do not capture any observed ensembles, we will not be able to infer the activity of these unobserved ensembles in the sessions where they are absent, because there are no observed ensembles linked through the dynamic prior.

3. To ensure uniqueness of the sparse decomposition of the dynamical systems model at each session and time point, we assume that the effective spark of the dynamics basis is large ($S^* \geq 2S$). Essentially, there is no $\boldsymbol{f}_k$ that can be linearly composed of $2S^*$ other dynamical systems. This ensures that there cannot exist two (or more) equivalent

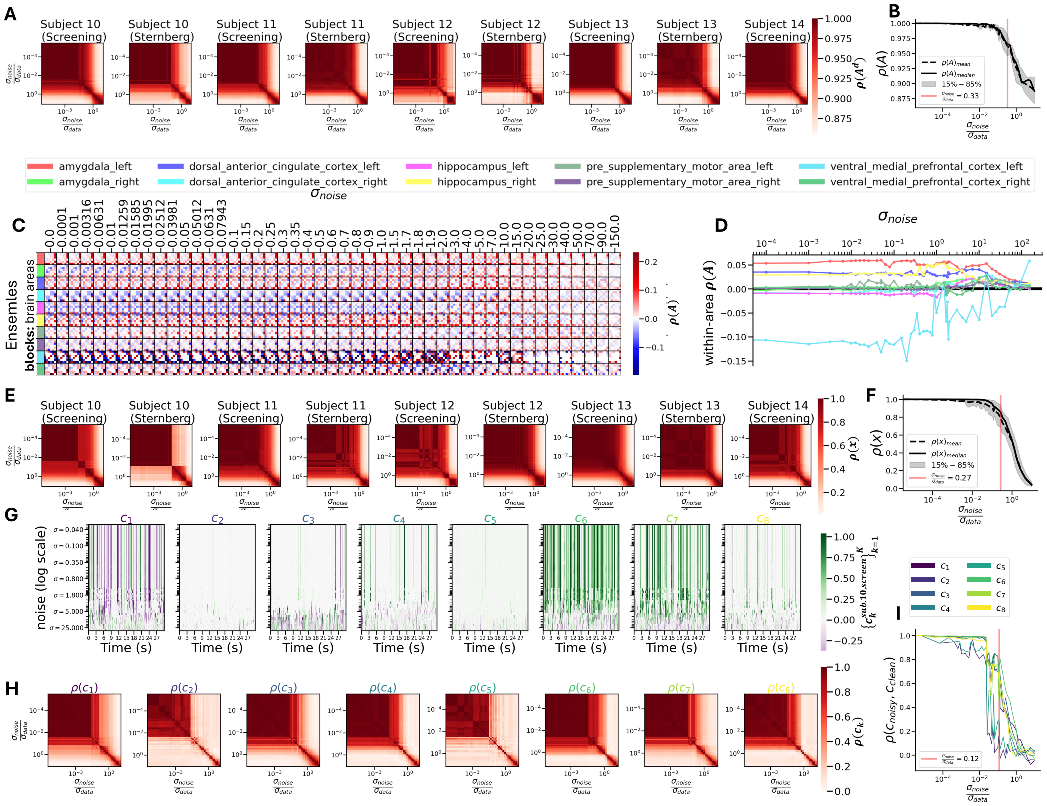

Figure 23: **CREIMBO's Robustness to Increasing Random Normal Noise Levels. A & B:** Correlations of identified ensemble compositions ($\boldsymbol{A}^d$) under increasing noise, for individual sessions (**A**) and all sessions combined (**B**). Robustness decreases only when $\frac{\sigma_{\text{noise}}}{\sigma_{\text{data}}} = \frac{1}{3}$. **C & D:** Correlations of ensemble compositions (from data concatenated across all conditions) displayed in a heatmap, with areas represented by rows of blocks (vertical) and noise levels by columns (horizontal). Block (i, j) captures the correlation of ensembles from area i at the j-th noise level. A sharp drop in within-area correlations (**D**) occurs at $\sigma_{\text{noise}} = 1$ ($\frac{\sigma_{\text{noise}}}{\sigma_{\text{data}}} \approx \frac{2}{3}$). **E & F:** Correlations of ensembles' trajectories ($\{\boldsymbol{x}^d\}_{d=1}^D$) for each condition (**E**) or combined (mean/median) (**F**) show robustness until $\frac{\sigma_{\text{noise}}}{\sigma_{\text{data}}} = 0.27$. **G:** Time-varying interaction coefficients for the 1st condition "(sub. 10, Screening)" under increasing noise reveal similar but more frequent changes, with a sharp frequency change at $\sigma_{\text{noise}} = 5$ ($\frac{\sigma_{\text{noise}}}{\sigma_{\text{data}}} = 0.33$). **H & I:** Correlations between corresponding $\{\boldsymbol{c}_k\}_{k=1}^K$ "(sub. 10, Screening)" over increasing noise (**H**), and compared to the coefficients identified from the original data (**H**).

decompositions $\sum_{k=1}^K \boldsymbol{f}_k c_{kt}$ and $\sum_{k=1}^K \boldsymbol{f}_k c_{kt}^*$ for distinct coefficients that both compose the same dynamical matrix.

4. Lastly, to ensure accurate cross-session alignment, we propose that each dynamical system projects uniquely onto the obseverved subset of ensembles in each session. This assumption prevents two dynamical systems (e.g., "ensemble 1 → ensemble 2 → ensemble 3" and "ensemble 1 → ensemble 4 → ensemble 3") from being indistinguishable from the data available in that session (e.g., a session with only ensembles 1 and 3 recorded).

E COMPUTATIONAL COMPLEXITY

CREIMBO's learning process involves learning both the ensemble compositions per session ($\{\boldsymbol{A}^d\}_{d=1}^D$), the ensembles' temporal activity ($\{\boldsymbol{x}_t^d\}_{d=1}^D$), and its underlying temporal evolution, which requires identifying the global (session-invariant) dynamic operators ($\{\boldsymbol{f}_j\}_{j=1}^J$) and their per-session temporal coefficients ($\{\boldsymbol{c}_t\}_{t=1}^T$).

Table 2: Parameter values for real-world human experiment

Parameter	Value	Explanation
same_c	False	Indicates if sub-circuit coefficients are shared across sessions.
step_f	0.2	Step size for gradient descent in updating $\boldsymbol{f}$.
GD_decay	0.992	Gradient descent step-size decay rate over iterations.
max_error	1×10^{-9}	Maximum allowable error.
max_iter	100	Maximum number of iterations.
seed	0	Random seed.
normalize_eig	True	Normalize eigenvalues.
start_sparse_c	False	Start with sparse $\boldsymbol{c}$.
include_D	True	Whether to include $\boldsymbol{A}$.
step_D	0.0001	Step size for updating $\boldsymbol{A}$.
num_gradient_steps	4	Number of gradient steps.
add_avg	True	Add average.
sparsity_on_f_max	45	Maximum sparsity on $\boldsymbol{f}$.
take_multiple_gd	False	Take multiple gradient descents.
D_graph_driven	True	Graph-driven $\boldsymbol{A}$.
infer_x_c_together	False	Infer $\boldsymbol{x}$ and $\boldsymbol{c}$ together.
include_mask	True	Include mask.
norm_D_cols	False	Normalize columns of $\boldsymbol{A}$.
lambda_D	0.3	Regularization parameter for $\boldsymbol{A}$.
step_D_decay	0.9999	Decay rate for step size of $\boldsymbol{A}$.
l1_D	2.74	ℓ_1 regularization for $\boldsymbol{A}$.

E.1 COMPLEXITY OF ENSEMBLE-MATRIX UPDATE

The loading matrix update relies on 4 main computational steps:

1) Channel Graph Construction: This operation, performed once for all N channels of every state $d = 1 \dots D$, generates a channel graph $\boldsymbol{H}^d \in \mathbb{R}^{N \times N}$ for each state $d \in [1, D]$ by concatenating within-state trials $1 \dots M_d$ horizontally, resulting in a $N \times \sum_{m=1}^{M_d} T_m^d$ matrix. For simplicity, let $\widetilde{T} = \sum_{m=1}^{M_d} T_m^d$. The computational complexity of calculating the pairwise similarities of this concatenated matrix for all D states is thus $\mathcal{O}\left(D\widetilde{T}^2 N(N-1)\right)$.

2) The k-threshold step: involves keeping only the k largest values in each row while setting the other values to zero—the complexity will be $\mathcal{O}\left(\widetilde{T}\log k\right)$ per row for a total computational complexity of $\mathcal{O}\left(DN\widetilde{T}\log k\right)$ for N rows and D states.

3) State Graph Construction: This is a one-time operation that involves calculating the pairwise similarities between each pair of states. For simplicity, if we assume the case of user-defined scalar labels, and as in this case there are D states (and accordingly D labels), the computation includes $D(D-1))/2$ pairwise distances for $\mathcal{O}\left(D^2\right)$.

4) Ensemble Inference (Eq. equation 1): This iterative step involves per-channel re-weighted ℓ_1 optimization. If the computational complexity of a weighted ℓ_1 is denoted as $\mathcal{C}$, then the computational complexity of the re-Weighted ℓ_1 Graph Filtering is $NL\mathcal{C} + LNk$, where N is the number of channels, L is the number of iterations for the RWLF procedure, and k is the number of nearest neighbors in the graph. For the last term in Eq. equation 1, there are p^2 multiplicative operations involving the vector ν and the difference in ensembles, arising from the ℓ_2^2 norm. Additionally, there is an additional multiplication step involving $\boldsymbol{P}_{dd'}$. For each state d, this calculation repeats itself $D-1$ times (for all $d' \neq d$). This process is carried out for every $d = 1 \dots D$. In total, these multiplicative operations sum up to $\left(p^2+1\right) D(D-1)$, resulting in a computational complexity of $\mathcal{O}\left(D^2 p^2\right)$.

E.2 COMPLEXITY OF INFERRING THE ENSEMBLES ACTIVITY AND INTERACTIONS COEFFICIENTS (EQ. EQUATION 2)

The inference of $\boldsymbol{c}_t^d$ for each $t = 1 \ldots T$ amd each condition $d = 1 \ldots D$, involves: $\widehat{\boldsymbol{c}}_t^d = \arg\min_{\boldsymbol{c}_t, \boldsymbol{x}_t} \|\boldsymbol{y}_t^d - \boldsymbol{a}\boldsymbol{x}_t\|_F^2 + \|\widetilde{\boldsymbol{x}_{t+1}}^d - \boldsymbol{F}\boldsymbol{X}_K^d \boldsymbol{c}_t^d\|_F^2 + \lambda_c \|\boldsymbol{c}_t\|_1$ where $\boldsymbol{F}\boldsymbol{X} \in \mathbb{R}^{p \times K}$ is the horizontal concatenation of $\{\boldsymbol{f}_k \boldsymbol{x}_{\boldsymbol{t}}\}_{k=1}^K$.

This simplifies to a Lasso problem of the form

$$\min_{\theta} \frac{1}{2} \|\xi - \mathcal{M}\theta\|^2 \quad \text{s.t.} \quad \|\theta\|_1 \leq \tau,$$

with dimensions $\xi : (N+p) \times 1$, $\mathcal{M} : (N+p) \times (p+K)$, and $\theta : (p+K) \times 1$, where

$$\xi = \begin{bmatrix} y_t \\ 0_{p \times 1} \end{bmatrix} \in \mathbb{R}^{(N+p) \times 1}, \quad \theta = \begin{bmatrix} x_t \\ c_t \end{bmatrix} \in \mathbb{R}^{(p+K) \times 1},$$

and

$$\mathcal{M} = \begin{bmatrix} A & 0_{N \times K} \\ I_p & \boldsymbol{F}\boldsymbol{X} \end{bmatrix} \in \mathbb{R}^{(N+p) \times (p+K)}.$$

This can be solved with SPGL1 with up to num_iters iterations, resulting in a computational complexity of

$$O(\text{num\_iters} \cdot (N+p)(p+K)).$$

per session and time point and overall (across all sessions and time points):

$$O(\text{num\_iters} \cdot (N+p)(p+K) \sum_{d=1}^{D} T^d).$$

E.3 COMPLEXITY OF INFERRING THE DYNAMICS' DICTIONARY

The inference of the basis-interactions dictionary $\{\boldsymbol{f}_k\}_{k=1}^K$ (via Eq. equation 3) involves solving

$$\widehat{\boldsymbol{F}}_{all} = \arg\min_{\boldsymbol{F}_{all}} \|\boldsymbol{x}^+ - \boldsymbol{F}_{all}(\boldsymbol{C}\boldsymbol{X})\|_F^2,$$

where $\boldsymbol{x}^+ \in \mathbb{R}^{p \times \sum_{d \in \text{batch}} \mathrm{T}^d}$ and $\boldsymbol{c}\boldsymbol{x} \in \mathbb{R}^{Kp \times \sum_{d \in \text{batch}} \mathrm{T}^d}$. For simplicity, assuming that $\lambda_\rho = 0$, The problem simplifies to a LASSO formulation, which is solved using SPGL1 for F^{all}, with an overall computational complexity per iteration of $O(\text{num\_iter} \cdot Kp^2\tau)$, where num_iter represents the number of iterations required for convergence.

F APPLICATION TO MULTI-REGIONAL CROSS-SESSION MICE NEURAL ACTIVITY

We further tested CREIMBO's ability to infer meaningful task variables underlying whole-brain multi-session data from mice Chen et al. (2023; 2024) while performing a memory-guided movement task. The measurements were obtained using multi-electrode extracellular electrophysiology, with the overall dataset stored in DANDI Archive under the NWB format Chen et al. (2023).

Particularly, the data include electrophysiology recordings of neural activity from multiple brain areas per session (Figs. 26, 27), across overall 175 sessions, with numerous trials in each. The task the mice performed during the recordings involved selecting one of two "lick ports" based on auditory cues, with the left or right port leading to a reward depending on whether they heard a high or low

Table 3: Parameter table for the CREIMBO on Mice Mesoscale.

Parameter	**Value**
max_error	1e-09
seed	0
normalize Fs	True
sparse_f	True
sparsity_on_f_max	40
increase_in_sparsity_f	1.4318632048860938
norm_D_cols	True
D_graph_params	{'with_kNN': True, 'with_norm': True, 'k': 15}
lambda_D	0.4392235894758376
update_type_D	spgl1
latent_dyns_initialization	random
D_with_lasso	True
l1_D	2.7440675196366238
params_D	{'update_c_type': 'spgl1'}
num_regions	10
reg_type_on_c	spgl1
lambda_x	1.0291322176748077
latent_dim	30
num ensembles per region	30
number of sub-dynamics	10
seed_f	0
sigma_mix_f	0.1
sparse_f_params	{'axis': '1', 'percent0': 20}

tone. Neural activity was recorded across several brain regions in each session, with some regions overlapping between sessions, though no two sessions had identical coverage (refer to Fig. 1., **A-B**, in Chen et al. (2024)).

We first loaded data from all sessions and selected areas for CREIMBO that featured the highest number of sessions including them. We identified the parent area of each sub-area labeled in the dataset and removed neurons with unlocated or NaN areas. Inspired by our exploratory analysis of parent-area distributions across sessions and neurons (Fig.27B,C), we selected the 10 parent areas with the highest number of neurons across sessions[1]. We then selected 20 random sessions. One of these 20 sessions contained only 'NaN'-located neurons, leaving 19 sessions for this analysis (Fig. 27D)[2].

We pre-processed the data using a 30 ms Gaussian kernel for firing rate estimation across all the sessions used (see F). We then selected only the neurons from the 10 parent areas and limited the analysis to the first 60 trials. Some sessions exhibited no activity or disconnection in certain trials, meaning some sessions included fewer than 60 trials (but no fewer than 40).

Next, we ran CREIMBO with 10 sub-circuits ($K = 10$) and $p_j = 3$ ensembles per area. The full list of parameters is shown in 3, and an example exploration of a random session is shown in (Fig.28,**A-C** show the firing rate, trial start-end times, and distribution of trial durations, respectively).

We identified ensembles per region (exemplary in 29A) with sub-circuits that capture both between-area (Fig.29C) and within-area interactions (Fig.29D), showing diverse motifs with varying degrees

---

[1] Used Parent Areas: Thalamus, Orbital Cortex, Secondary Motor Cortex, Basal Ganglia, Olfactory Cortex, Brain Stem, Somatosensory Cortex, Frontal Cortex, Hippocampus, Primary Motor Cortex

[2] Sessions DANDI names: '78a58614-09e4-4e29-a492-8bbeaf7a8cf6', 'ab103954-d99f-46b1-98ac-e6f91a1e9313', '32701cfa-8932-4d9b-9f4d-cc05cb22ae89', 'b080c738-17c9-4e0d-aee4-6d5371518f69', '886c4302-846a-4ef5-996a-6f02d6a81a5f', 'ba5b1ff3-753e-425c-baf0-e7cdd0c08093', 'ea856208-4240-404a-9034-d729ad6f4cda', 'ed759efa-dceb-4472-a2a3-4f7357d67665', '8a2ce9b2-2e98-4c37-8f2a-3b9c8b542086', '22791d80-26dc-4495-b4c0-651fe10e3298', 'a007fac1-96e7-4028-ad84-31a1b80db089', 'b39eb52a-0774-411b-b374-6eb08a73562e', '8dbc25ee-cc17-4504-a1b9-7d43643b9466', '981feb84-f209-4994-8838-02a0048feb87', '585dc9d4-be9c-4244-8fa7-e64309019afc', 'aa74e4d7-a79b-4179-adf3-497fb1237edc', 'ebfab58b-7c80-4f31-9b4e-2b33883bb14a', '8c724097-3876-48fc-94e0-832779e4f1be', '2e9cb8a1-457d-49ea-97fd-f7023434d231'

of cross-circuit correlations (Fig. 29B). Some cross-area interactions reveal effects originating from specific regions involved in the task. For example, $\boldsymbol{f}_1$ demonstrates hippocampal effects, which align with the task's memory demands, while, e.g., $\boldsymbol{f}_3$ shows interactions involving the frontal cortex, including follow-up activations, corresponding to the task's need for planning and execution. Other sub-circuits reveal inputs converging on specific areas. For instance, $\boldsymbol{f}_8$ shows motor cortex inputs, relevant for moving the tongue during the lick response, and $\boldsymbol{f}_2$ reflects inputs into the secondary motor cortex, which is involved in coordinating motor actions.

When extracting only within-area interactions, we observe unique motifs as well. For example, $\boldsymbol{f}_1$ shows further internal processing between basal ganglia ensembles, which may reflect the internal coordination and integration of motor planning and execution signals. $\boldsymbol{f}_7$ and $\boldsymbol{f}_2$ show strong effects of one ensemble on another within the secondary motor cortex, which could represent the modulation and refinement of motor commands for more precise movements. $\boldsymbol{f}_5$ demonstrates brainstem effects, with two ensembles influencing two other ensembles, potentially supporting basic motor functions such as muscle activation and coordination. $\boldsymbol{f}_4$ shows multiple self-activations of ensembles, which may capture self-regulatory processes like feedback inhibition or facilitation that modulate motor output and prevent over-activation.

We further examined CREIMBO's dynamics coefficients ($\boldsymbol{c}_t$) and identified task-related patterns with similar coefficient profiles across trials for the same task variable (Fig 4A for an example session, and B for hit vs. miss outcomes). Similar differences were observed across other task variables. To quantify the predictive power of the dynamic coefficients, we used them as input for training a simple one-vs-rest logistic regression classifier. Each trial was split into four equal-duration time windows, and the 10 dynamic coefficients were averaged within each window, resulting in 40 features (4 windows × 10 coefficients). These features were then used to predict task variables, including outcome (hit/miss/ignore), early lick (whether a lick was early), lick side instructed, and lick side performed in practice. Additionally, we tested the model to predict 2-3 variables simultaneously, which was more challenging due to the need to distinguish between multiple options. The resulting accuracy levels (Fig 4C, black stars) were significantly higher than chance levels (gray bars). We further analyzed the confusion matrix for each variable's prediction and applied the χ^2 test to assess whether the distribution of predictions significantly deviated from the expected distribution under chance. We found p-values well below 1×10^{-10} (see subtitles of Fig 4D, F, G, H, I, J), strongly supporting CREIMBO's predictive power.

Furthermore, we assessed the importance of subcircuits' activations across the four time windows (Fig.29E), with each block of rows representing one subcircuit and the blocks corresponding to different time windows. CREIMBO revealed patterns where certain time windows and dynamic coefficients were pivotal for different task variables. For instance, c_7 at t_3 was critical, while other coefficients, like c_9 at t_3, were specific to encoding the lick side. This specificity aligns with the fact that this time point likely reflects the final stages of processing during the task, including aspects of learning. When we examined c_9 (Fig.29C), we observed multiple inputs into the secondary motor cortex, related to the execution of the lick towards the trial's end, highlighting CREIMBO's ability to pinpoint region-specific interactions. Additionally, c_8 showed increased importance in the initial window t_0, contributing across multiple variables and capturing inputs into the hippocampus—an area integral to memory processing—underscoring its role in early trial stages. These findings further validate CREIMBO's ability to capture and predict task-related neural dynamics, offering insights into circuit-level brain activity across time.

G INFERENCE ASSUMING POISSON STATISTICS

CREIMBO, as outlined in the main text, assumes Gaussian-distributed *i.i.d* noise. This assumption is reflected in the inference procedure, which minimizes the ℓ_2 and Frobenius norms (e.g., equation 1, equation 2). Particularly, these norms arise from minimizing the negative log-likelihood of Gaussian-distributed observations noise ($p(\boldsymbol{Y}^d_{n,t}) = \frac{1}{\sqrt{2\pi\sigma^2}} \exp\left(-\frac{\boldsymbol{Y}^d_{n,t} - [A^d X^d]_{n,t})^2}{2\sigma^2}\right)$, with some noise standard-deviation σ.

Electrophysiology, however, records trains of action potentials (spikes) that are often modeled as a Poisson processes. Binned spike counts are thus typically approximated as a Poisson random variable. However, when firing rates (FRs) are high enough, the Gaussian assumption is an adequate approximation, and thus the Gaussian assumption remains common in data-driven neuroscience models (e.g., Linderman et al. (2016); Aoi & Pillow (2018)). However, some species (e.g., bats (Allen et al., 2021)) exhibit extremely low FRs, which may require Poisson likelihood functions. Thus we propose an extension to CREIMBO that with a Poisson likelihood function for ensemble and traces inference, that can replace the Gaussian model in low spiking-rates scenarios.

Our Poisson extension first involves transforming the spike-timing data to binned spike counts for all sessions $d = 1 \dots D$ ($\{\boldsymbol{Y}^d\}_{d=1}^D$). Next, we consider the same goal of finding the ensembles $\boldsymbol{A}^d$ and their traces $(\boldsymbol{X}^T)^d$, under the assumption that the data follows a Poisson distribution.

To simplify, we focus on a single session d, with $\boldsymbol{y} = (\boldsymbol{Y}^d)^T$ (T for transpose), and note that the extension below applies to all sessions. In the Poisson model, for each neuron $n = 1 \dots N$, the likelihood of a certain spike count at time t given a latent rate $\lambda_{t,n}$ is:

$$p(\boldsymbol{y_{t,n}}|\lambda_{t,n}) = \frac{\lambda_{t,n}^{y_{t,n}} e^{-\lambda_{t,n}}}{y_{t,n}!}$$

where $y_{t,n}!$ denotes the factorial of $y_{t,n}$.

Here we model the unknown rate $\boldsymbol{\lambda} \in \mathbb{R}^{T \times N}$ as the low-dimensional representation captured via the ensembles $\boldsymbol{A}^d \in \mathbb{R}^{N \times p}$ and their traces $\widetilde{\boldsymbol{x}} := (\boldsymbol{X}^d)^T \in \mathbb{R}^{T \times p}$ (T for transpose), i.e., $\boldsymbol{\lambda} = \boldsymbol{A}^d \boldsymbol{X}^d$, such that the likelihood becomes

$$\begin{aligned} p(\boldsymbol{y}|\widetilde{\boldsymbol{x}}, \boldsymbol{A}) &= \prod_{n=1}^{N} \prod_{t=1}^{T} p(y_{t,n}|\lambda_{t,n}) \\ &= \prod_{n=1}^{N} \prod_{t=1}^{T} p(y_{t,n}|[\widetilde{\boldsymbol{x}} \boldsymbol{A}^T]_{t,n}) \\ &= \prod_{n=1}^{N} \prod_{t=1}^{T} \frac{([\widetilde{\boldsymbol{x}} \boldsymbol{A}^T]_{t,n})^{y_{t,n}} e^{-([\widetilde{\boldsymbol{x}} \boldsymbol{A}^T]_{t,n})}}{y_{t,n}!}. \end{aligned}$$

This can be trained by iteratively updating $\widetilde{\boldsymbol{x}}$ and $\boldsymbol{A}$ to minimize the negative log of the above likelihood, which can be represented mathematically as:

$$\begin{aligned} \{\widehat{\widetilde{\boldsymbol{x}}}, \widehat{\boldsymbol{A}}\} &= \arg\min_{\widetilde{\boldsymbol{x}}, \boldsymbol{A}} \left[-log \left(\prod_{n=1}^{N} \prod_{t=1}^{T} \frac{([\widetilde{\boldsymbol{x}} \boldsymbol{A}^T]_{t,n})^{y_{t,n}} e^{-([\widetilde{\boldsymbol{x}} \boldsymbol{A}^T]_{t,n})}}{y_{t,n}!} \right) \right] \\ &= \arg\min_{\widetilde{\boldsymbol{x}}, \boldsymbol{A}} \sum_{n=1}^{N} \sum_{t=1}^{T} \left[[\widetilde{\boldsymbol{x}} \boldsymbol{A}^T]_{t,n} - y_{t,n} \log([\widetilde{\boldsymbol{x}} \boldsymbol{A}^T]_{t,n}) \right] \end{aligned} \tag{4}$$

where the logarithm is taken using the natural exponential base. Notably, in the above $\arg\min$, we chose to omit the constant term that emerge from taking the logarithm (i.e., $log(y_{t,n}!)$) as it does not affect the argument minimization.

In this Poisson case, in contrast to the Gaussian, we can no longer solve for $\boldsymbol{x}$ using e.g., least squares or LASSO; instead, we will update $\widetilde{\boldsymbol{x}}$ via Gradient Descent. The first step is to compute the gradient of the cost function in equation 4 with respect to $\widetilde{\boldsymbol{x}}$.

To simplify the calculation, we first notate the two components obtained in equation 4 by the auxiliary terms

$$g_1(\widetilde{\boldsymbol{x}}, \boldsymbol{A}) = \sum_{t,n} [\widetilde{\boldsymbol{x}} \boldsymbol{A}^T]_{t,n}$$

and

$$g_2(\boldsymbol{y}, \widetilde{\boldsymbol{x}}, \boldsymbol{A}) = \sum_{t,n} -y_{t,n} \cdot \log([\widetilde{\boldsymbol{x}} \boldsymbol{A}^T]_{t,n}).$$

The cost function from equation 4 thus can be written in terms of these functions as:

$$\{\widehat{\widetilde{\boldsymbol{x}}}, \widehat{\boldsymbol{A}}\} = \arg\min_{\widetilde{\boldsymbol{x}}, \boldsymbol{A}} \left[g_1(\widetilde{\boldsymbol{x}}, \boldsymbol{A}) + g_2(\boldsymbol{y}, \widetilde{\boldsymbol{x}}, \boldsymbol{A})\right]. \tag{5}$$

Hence, for updating $\widetilde{\boldsymbol{x}}$ via Gradient Descent, we need to find the gradients of g_1 and g_2.

We first establish two notations to make subsequent steps clearer:

- let $[1]_{(m,k)}$ denote a matrix of ones of size $m \times k$.
- let $\delta_{(M,P)_{m,p}}$ denote a matrix of shape $M \times P$ whose entries are all zeros except for the entry at index (m, p), which is set to 1.

Calculate $\frac{\partial g_1(\widetilde{\boldsymbol{x}}, \boldsymbol{A})}{\partial \widetilde{\boldsymbol{x}}}$:

To begin, we can rewrite $g_1(\widetilde{\boldsymbol{x}}, \boldsymbol{A})$ as

$$g_1(\widetilde{\boldsymbol{x}}, \boldsymbol{A}) = \sum_{t,n} [\widetilde{\boldsymbol{x}}\boldsymbol{A}^T]_{t,n} = [1]_{(1,T)} \widetilde{\boldsymbol{x}}\boldsymbol{A}^T [1]_{(N,1)}$$

and follow the identity (taken from Petersen et al. (2008) Eq. 20):

$$\frac{\partial [\boldsymbol{a}^T \boldsymbol{M} \boldsymbol{b}]}{\partial \boldsymbol{M}} = \boldsymbol{a}\boldsymbol{b}^T \quad \text{where } \boldsymbol{a}, \boldsymbol{b} \text{ vectors, and } \boldsymbol{M} \text{ matrix.} \tag{6}$$

Building on this, let $[1]_{(1,T)}$ correspond to the $\boldsymbol{a}^T$ vector from equation 6, $\boldsymbol{A}^T[1]_{(N,1)} \in \mathbb{R}^{p \times 1}$ correspond to the $\boldsymbol{b}$ vector of equation 6, and $\widetilde{\boldsymbol{x}}$ correspond to the matrix $\boldsymbol{M}$. Then, the gradient of $g_1(\widetilde{\boldsymbol{x}}, \boldsymbol{A})$ with respect to $\widetilde{\boldsymbol{x}}$ is:

$$\frac{\partial g_1(\widetilde{\boldsymbol{x}}, \boldsymbol{A})}{\partial \widetilde{\boldsymbol{x}}} = \frac{\partial \left([1]_{(1,T)} \widetilde{\boldsymbol{x}}\boldsymbol{A}^T [1]_{(N,1)}\right)}{\partial \widetilde{\boldsymbol{x}}} = [1]_{(T,1)}[1]_{(1,N)}\boldsymbol{A} = [1]_{(T,N)}\boldsymbol{A}$$

Calculate $\frac{\partial g_2(\boldsymbol{y}, \widetilde{\boldsymbol{x}}, \boldsymbol{A})}{\partial \widetilde{\boldsymbol{x}}}$:

First, we will rewrite the term $[\widetilde{\boldsymbol{x}}\boldsymbol{A}^T]_{t,n}$ as:

$$[\widetilde{\boldsymbol{x}}\boldsymbol{A}^T]_{t,n} = \sum_{j=1}^{p} \widetilde{\boldsymbol{x}}_{t,j} (\boldsymbol{A}^T)_{j,n} = \delta_{(1,T)_{1,t}} \widetilde{\boldsymbol{x}}\boldsymbol{A}^T \delta_{(N,1)_{n,1}} \tag{7}$$

$\delta_{(1,T)_{1,t}}$ is a row vector of length T with a value of 1 at index t and 0 elsewhere, and $\delta_{(N,1)_{n,1}}$ is a column vector of length N with a value of 1 at index n and 0 elsewhere.

We will use again the identity from Petersen et al. (2008) presented in equation 6, and now mark $\delta_{(1,T)_{1,n}}$ with the equation 6's vector $\boldsymbol{a}^T$, $\widetilde{\boldsymbol{x}}$ is again $\boldsymbol{M}$, and $b := \boldsymbol{A}^T \delta_{(N,1)_{j,1}}$. When applying the identity in equation 6 to equation 7, we thus obtain

$$\frac{\partial [\widetilde{\boldsymbol{x}}\boldsymbol{A}^T]_{t,n}}{\partial \widetilde{\boldsymbol{x}}} = \delta_{(T,1)_{t,1}} \delta_{(1,N)_{1,n}} \boldsymbol{A} = \delta_{(T,N)_{t,n}} \boldsymbol{A}$$

Given the above, we receive

$$\begin{aligned}
\frac{\partial g_2(\boldsymbol{y}, \widetilde{\boldsymbol{x}}, \boldsymbol{A})}{\partial \widetilde{\boldsymbol{x}}} &= \frac{\partial \left(\sum_{n=1}^{N} \sum_{t=1}^{T} -y_{t,n} \log\left([\widetilde{\boldsymbol{x}}\boldsymbol{A}^T]_{t,n}\right)\right)}{\partial \widetilde{\boldsymbol{x}}} \\
&= -\sum_{n=1}^{N} \sum_{t=1}^{T} \frac{y_{tn}}{[\widetilde{\boldsymbol{x}}\boldsymbol{A}^T]_{t,n}} \delta_{(T,N)_{t,n}} \boldsymbol{A} \\
&= -\sum_{t,n} \psi_{t,n} \delta_{(T,N)_{t,n}} \boldsymbol{A} \\
&= -\left(\sum_{t,n} \psi_{t,n} \delta_{(T,N)_{t,n}}\right) \boldsymbol{A} \\
&= -\boldsymbol{\Psi}\boldsymbol{A}
\end{aligned} \tag{8}$$

where $\psi_{t,n} = \frac{y_{t,n}}{[\widetilde{\boldsymbol{x}}\boldsymbol{A}^T]_{t,n}}$, and $\boldsymbol{\Psi} \in \mathbb{R}^{T \times N}$ is a matrix whose entry at index (t, n) is $\psi_{t,n}$.

Going back to the expression in equation 5, the full gradient of the Poisson loss with respect to $\widetilde{\boldsymbol{x}}$ is:

$$\frac{\partial[g_1(\widetilde{\boldsymbol{x}}, \boldsymbol{A}) + g_2(\boldsymbol{y}, \widetilde{\boldsymbol{x}}, \boldsymbol{A})]}{\partial \widetilde{\boldsymbol{x}}} = [1]_{(T,N)}\boldsymbol{A} - \boldsymbol{\Psi}\boldsymbol{A} = ([1]_{(T,N)} - \boldsymbol{\Psi})\boldsymbol{A},$$

and the projected gradient step in $\widetilde{\boldsymbol{x}}$ at iteration m thus follows:

$$\widetilde{\boldsymbol{x}}^{m+1} \leftarrow \Pi\left(\widetilde{\boldsymbol{x}}^m - \eta^m \left([1]_{(T,N)} - \boldsymbol{\Psi}\right)\boldsymbol{A}\right)$$

where Π can project the columns of $\widetilde{\boldsymbol{x}}$ onto some constraint set, with the identity transform used if no projection is desired, and η^m is the gradient descent step size at iteration m.

For inferring $\boldsymbol{A}$, at each iteration m, we can then use the Spiral-Tap package Harmany et al. (2012) to infer the sparse ensembles.

The above ensemble model (including $\boldsymbol{A}$ and $\boldsymbol{x}$) is the only part that directly connects to the Poisson-distributed spike-counts ($\boldsymbol{Y}^d$), while the latent evolution of $\boldsymbol{x}$ via $x_t = \boldsymbol{F}_t\boldsymbol{x}_{t-1}$ is independent of the Poisson assumption on the spike-counts $\boldsymbol{Y}^d$. Particularly, as the transition from $\boldsymbol{x_t}$ to $\boldsymbol{x_{t+1}}$ is dictated by the ensembles' dynamic interactions ($\boldsymbol{F_t} = \sum_{k=1}^K c_{kt}\boldsymbol{f}_k$), which we continue to assume follows a Gaussian distribution in the latent space, the dynamic inference part of CREIMBO remains unchanged from the main text.

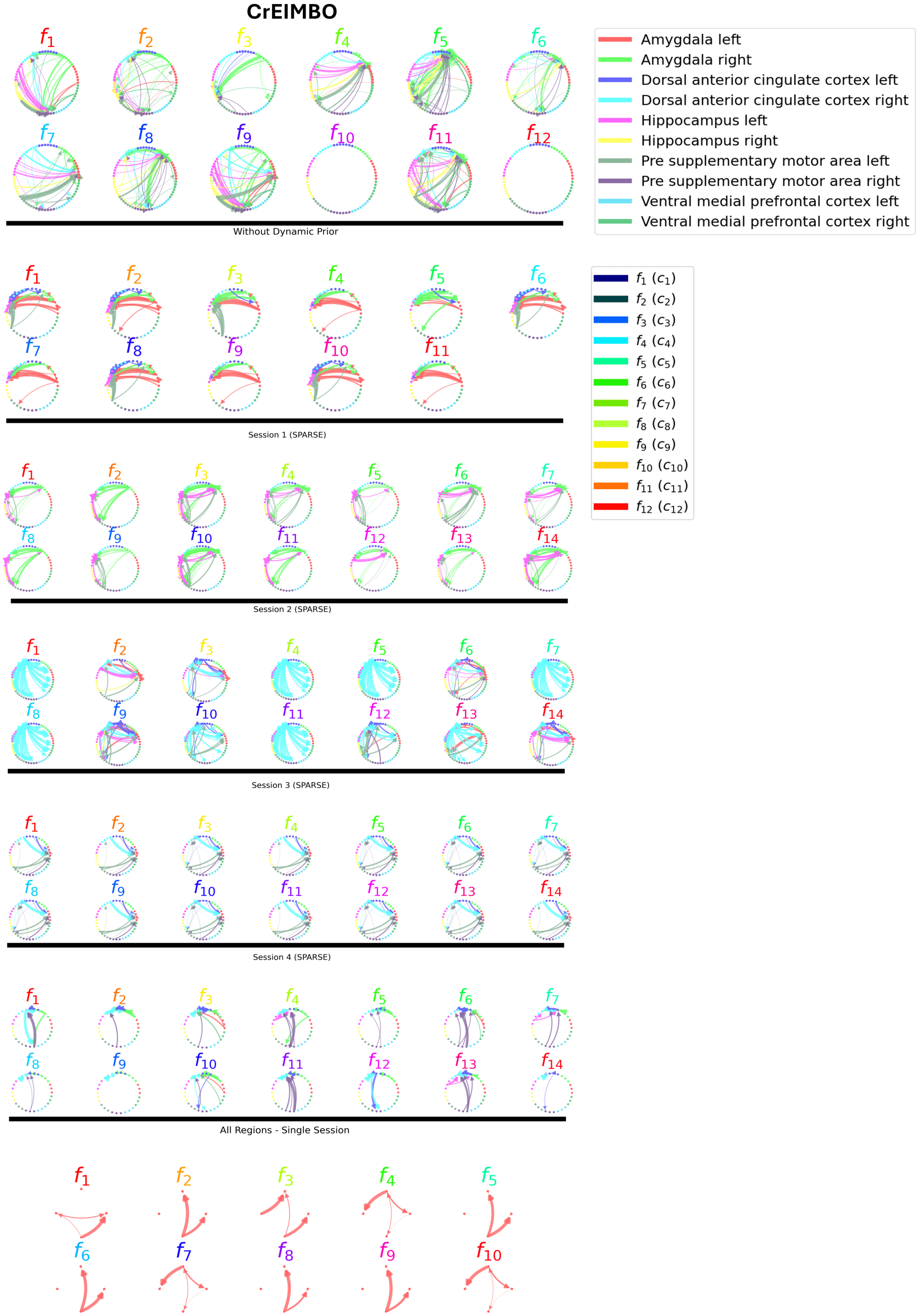
CrEIMBO
f_1 f_2 f_3 f_4 f_5 f_6
f_7 f_8 f_9 f_{10} f_{11} f_{12}
Amygdala left
Amygdala right
Dorsal anterior cingulate cortex left
Dorsal anterior cingulate cortex right
Hippocampus left
Hippocampus right
Pre supplementary motor area left
Pre supplementary motor area right
Ventral medial prefrontal cortex left
Ventral medial prefrontal cortex right
Without Dynamic Prior
f_1 f_2 f_3 f_4 f_5 f_6
f_7 f_8 f_9 f_{10} f_{11}
f_1 (c_1)
f_2 (c_2)
f_3 (c_3)
f_4 (c_4)
f_5 (c_5)
f_6 (c_6)
f_7 (c_7)
f_8 (c_8)
f_9 (c_9)
f_{10} (c_{10})
f_{11} (c_{11})
f_{12} (c_{12})
Session 1 (SPARSE)
f_1 f_2 f_3 f_4 f_5 f_6 f_7
f_8 f_9 f_{10} f_{11} f_{12} f_{13} f_{14}
Session 2 (SPARSE)
f_1 f_2 f_3 f_4 f_5 f_6 f_7
f_8 f_9 f_{10} f_{11} f_{12} f_{13} f_{14}
Session 3 (SPARSE)
f_1 f_2 f_3 f_4 f_5 f_6 f_7
f_8 f_9 f_{10} f_{11} f_{12} f_{13} f_{14}
Session 4 (SPARSE)
f_1 f_2 f_3 f_4 f_5 f_6 f_7
f_8 f_9 f_{10} f_{11} f_{12} f_{13} f_{14}
All Regions - Single Session
f_1 f_2 f_3 f_4 f_5
f_6 f_7 f_8 f_9 f_{10}

Figure 24: Comparison of sub-circuits identified by CREIMBO with those identified by other approaches using the real-world human neural recordings. CREIMBO reveals distinct motifs capturing multi-regional flows to specific areas, including both cross-regional and multi-regional interactions. In contrast, other approaches identify sub-circuits with overlapping flows that fail to capture the full spectrum of multi-regional interactions.

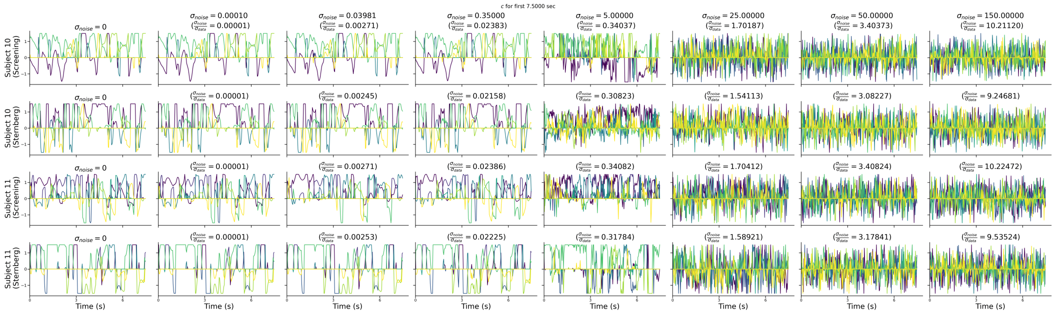

Figure 25: Identified dynamics' coefficients ($c_{k=1}^{K}$) for the human data experiment under increasing noise levels demonstrate robustness, with a rapid increase in internal pattern frequency at higher noise levels.

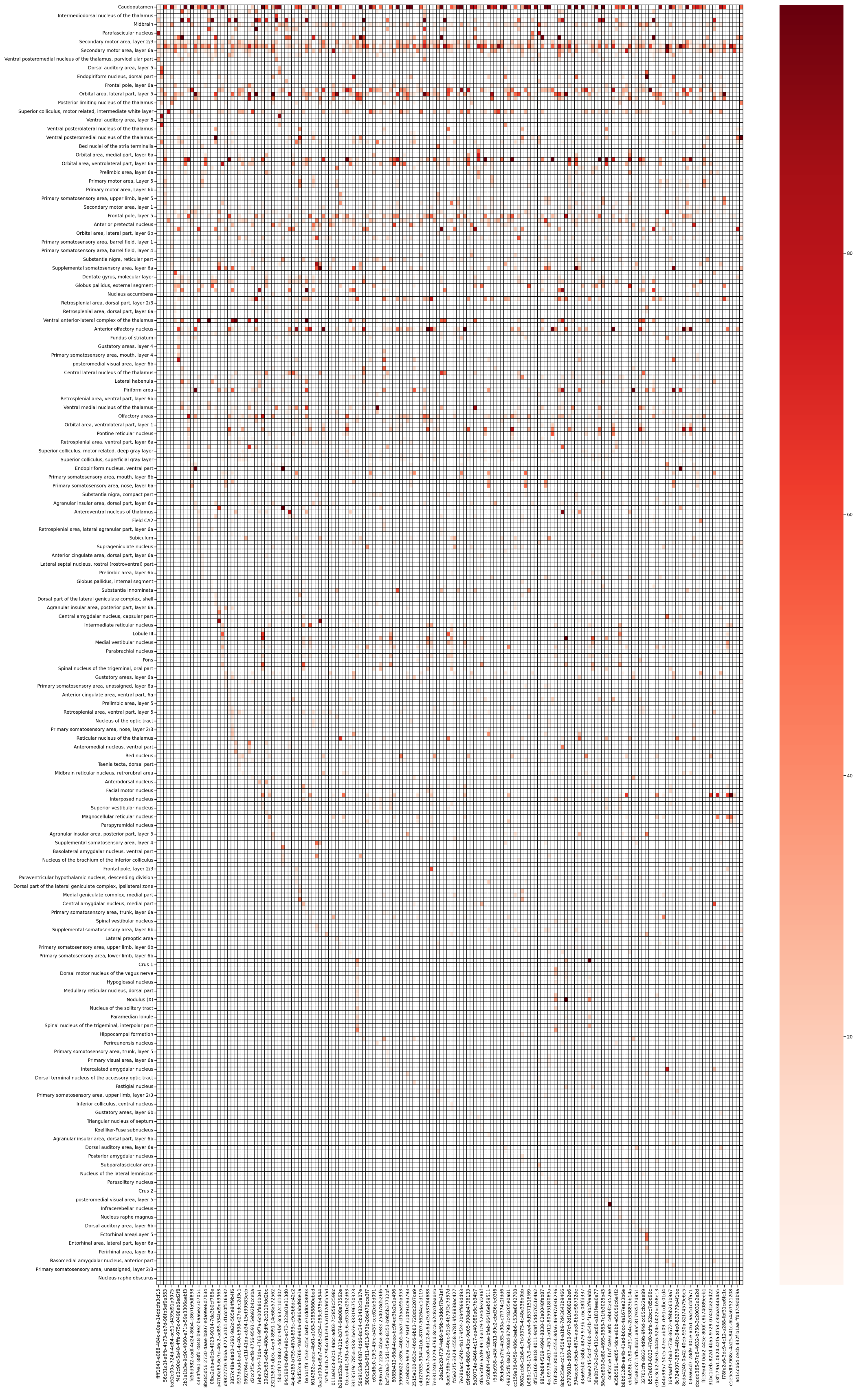

Figure 26: number of neurons per area across all files

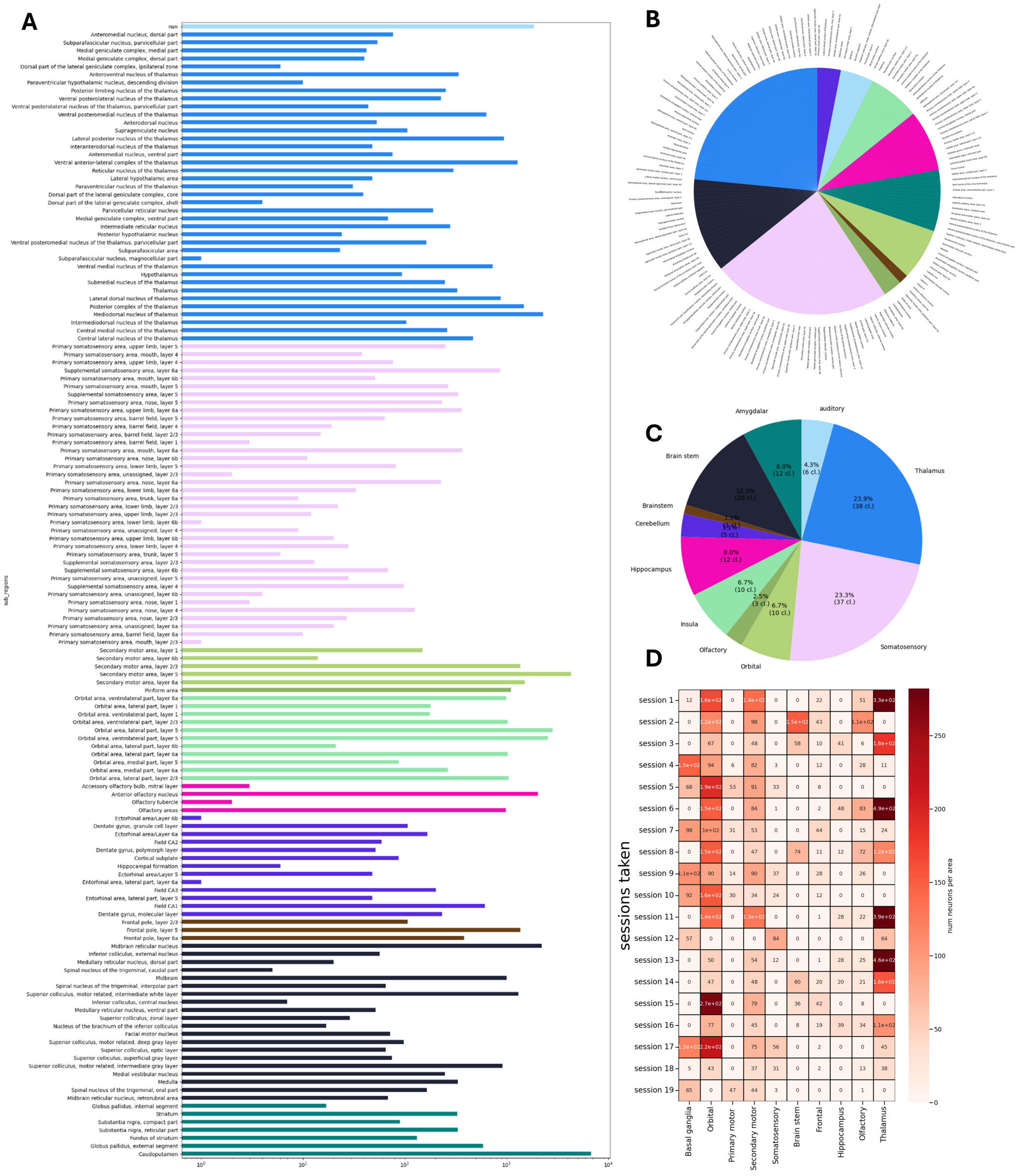

	Basal ganglia	Orbital	Primary motor	Secondary motor	Somatosensory	Brain stem	Frontal	Hippocampus	Olfactory	Thalamus
session 1	12	1.6e+02	0	1.4e+02	0	0	22	0	51	3.3e+02
session 2	0	1.2e+02	0	98	0	1.5e+02	43	0	1.1e+02	0
session 3	0	67	0	48	0	58	10	41	6	1.8e+02
session 4	1.5e+02	94	6	82	3	0	12	0	28	11
session 5	68	1.9e+02	53	91	33	0	8	0	0	0
session 6	0	1.5e+02	0	84	1	0	2	48	83	4.9e+02
session 7	98	1e+02	31	53	0	0	44	0	15	24
session 8	0	1.5e+02	0	47	0	74	11	12	72	1.2e+02
session 9	1.1e+02	90	14	90	37	0	28	0	26	0
session 10	92	1.6e+02	30	34	24	0	12	0	0	0
session 11	0	1.4e+02	0	1.3e+02	0	0	1	28	22	3.9e+02
session 12	57	0	0	0	84	0	0	0	0	64
session 13	0	50	0	54	12	0	1	28	25	4.6e+02
session 14	0	47	0	48	0	60	20	20	21	1.6e+02
session 15	0	2.7e+02	0	79	0	36	42	0	8	0
session 16	0	77	0	45	0	8	19	39	34	1.1e+02
session 17	1.2e+02	2.2e+02	0	75	56	0	2	0	0	45
session 18	5	43	0	37	31	0	2	0	13	38
session 19	65	0	47	44	3	0	0	0	1	0

Figure 27: number of neurons per area as a motivation for area-focusing. **A:** Overall number of neurons per sub-area (colored by parent area) across all sessions. **B:** Distribution of areas with sub-area name across all sessions. **C:** Distribution of areas with parent-area name across all sessions. **D:** Number of neurons per parent-area (across the 10 selected areas) in the 19 used sessions.

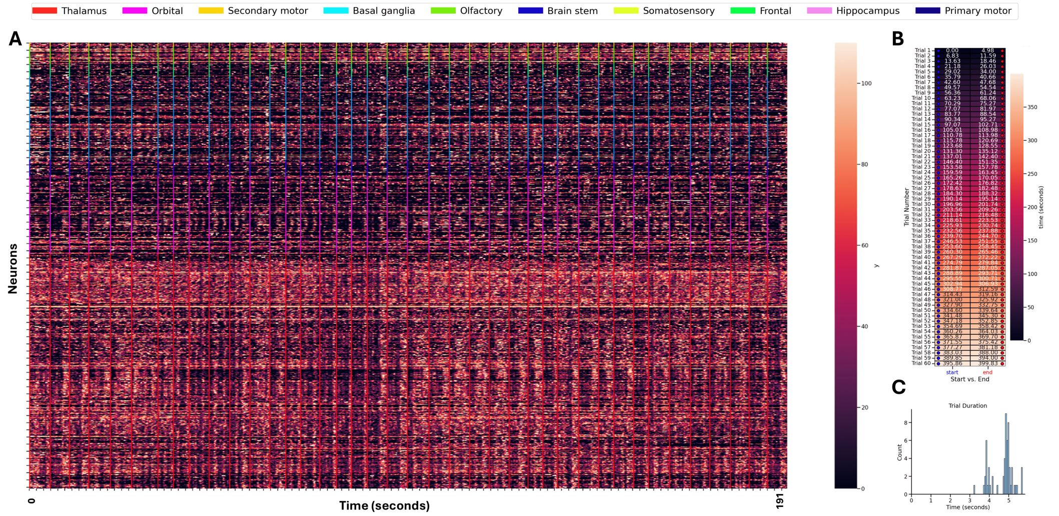

Figure 28: Example Session Chen et al. (2024). **A:** Data firing rate over time separated by trials in vertical lines. the color of the vertical line captures the relevant brain area (example random session). **B:** Trials start and end times (in seconds) for examples session. **C:** Trial duration distribution for example random session.

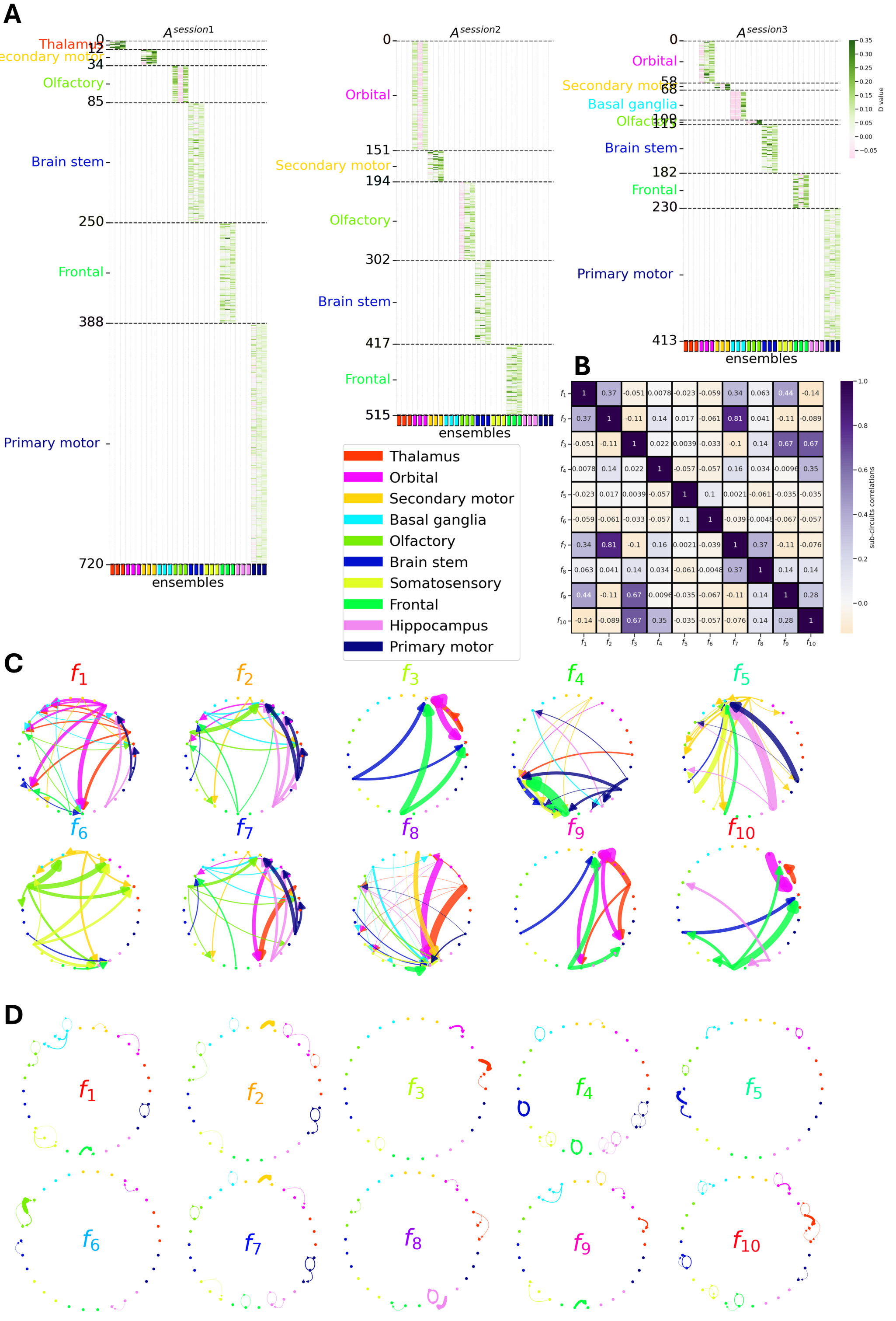

Figure 29: Identified components of the Mesoscale data (Chen et al., 2024) using 19 random sessions with 40-60 trials within each. **A:** Identified ensemble matrices for three random sessions. **B:** Correlations between circuits. **C:** Between-areas interactions (extracted from $\{\boldsymbol{f}_k\}_{k=1}^{K}$ via a block off-diagonal mask) **D:** Within-areas interactions (extracted from $\{\boldsymbol{f}_k\}_{k=1}^{K}$ via a block diagonal mask)